JGR Oceans

RESEARCH ARTICLE
10.1029/2019JC015227

Key Points:
- The EAC intensifies and deepens towards the separation zone, to a maximum mean poleward transport of 26.8 Sv, then broadens and shallows
- Eddy driven transport over the separation region has a strong annual modulation, related to the annual cycle in eddy kinetic energy
- Mesoscale eddy variability stems from both intrinsic instabilities of the EAC jet and westward propagating Rossby waves from remote source

Correspondence to:
C. Kerry,
c.kerry@unsw.edu.au

Citation:
Kerry, C. G., & Roughan, M. (2020). Downstream evolution of the east Australian Current system: mean flow, seasonal, and intra-annual variability. *Journal of Geophysical Research: Oceans*, *125*, e2019JC015227. https://doi.org/10.1029/2019JC015227

Received 16 APR 2019
Accepted 20 MAR 2020
Accepted article online 24 MAR 2020

Downstream Evolution of the East Australian Current System: Mean Flow, Seasonal, and Intra-annual Variability

Colette Kerry[1] **and Moninya Roughan**[1]

[1]Coastal and Regional Oceanography Lab, School of Mathematics and Statistics, UNSW Australia, Sydney, NSW, Australia

Abstract The East Australian Current (EAC) varies on both seasonal and mesoscale eddy related timescales, with important impacts for weather, primary productivity, and fisheries. While the EAC and its eddies have been the subject of many synoptic studies, a consistent three-dimensional picture of the current, its downstream evolution, and the associated seasonal and intra-annual variability is lacking. We use a 22-year model simulation to quantify the EAC's temporal and latitudinal variability, from where it flows as a mostly coherent jet (27° S) to its separation from the coast (31–33° S), its energetic eddy field in the Tasman Sea and its southern extension. We show that the current intensifies and deepens poleward toward the separation latitude; the mean poleward transport reaches a maximum of 26.8 Sv and the seasonal cycle amplitude peaks at 6.2 Sv. Over the separation region, the EAC core broadens and shallows, mean poleward transport is lower and the transport standard deviation peaks at 22.0 Sv. The meandering EAC jet is modulated at interannual timescales, while the eddy driven transport over the separation region has a strong annual modulation, related to the annual cycle in eddy kinetic energy. SSH variability at intra-annual frequencies is described primarily by an alongshore propagating mode and an onshore propagating mode, demonstrating that mesoscale SSH variability stems from a combination of intrinsic instabilities of the EAC jet and westward propagating Rossby waves. The results provide the first holistic analysis of the EAC system along its latitudinal range.

1. Introduction

The East Australian Current (EAC) is the Western Boundary Current (WBC) of the South Pacific subtropical gyre, flowing poleward along the east coast of Australia. The EAC has the weakest mean flow of the WBCs associated with the subtropical gyres (Mata et al., 2000) but its flow is characterized by high eddy variability (Mata et al., 2006) comparable with stronger WBCs such as the Gulf Stream, the Kuroshio, and the Agulhas Current (e.g., Feron, 1995; Gordon et al., 1983). The EAC forms in the South Coral Sea (15–24° S) where the westward flow of the subtropical gyre, the South Equatorial Current, separates into a series of jets that feed the poleward flowing EAC (Ganachaud et al., 2014). The current strengthens and separates from the coast between 31° S and 33° S (Cetina Heredia et al., 2014). Turning eastward, the current sheds large anticyclonic and cyclonic eddies in the Tasman Sea (Oke & Middleton, 2000), with a portion of the flow continuing southwards (Ridgway & Dunn, 2003). A recent review paper by Oke, Roughan, et al. (2019) describes the EAC as it transitions from a continuous, poleward-flowing current adjacent to the coast (the EAC jet), to a complex field of eddies after separation (the EAC eddy field). The mesoscale eddies feed flow to the east toward New Zealand (the EAC eastern extension) and southwards toward Tasmania (the EAC southern extension), flow features that are evident only in the time-averaged fields (Oke, Pilo, et al., 2019). While the eastward flow has traditionally been referred to as the Tasman Front, Oke, Roughan, et al. (2019) show that the flow between Australia and New Zealand follows multiple paths and is much broader than the label "Tasman Front" suggests. As such, they recommend the use of the term "the EAC eastern extension"—since this does not imply the presence of a front. Accordingly, they suggest that the southward flow, traditionally referred to as the EAC extension, be referred to as "the EAC southern extension." We follow this revised naming convention. A mean northward return flow of the EAC jet appears offshore in the mean fields. This description of the EAC system is depicted in Figure 1.

Eddies form in all parts of the EAC region, as far north as 25° S (Qiu & Chen, 2004), with the greatest eddy kinetic energy (EKE) occurring between 32° S and 35° S (Bowen et al., 2005). A variety of mechanisms have

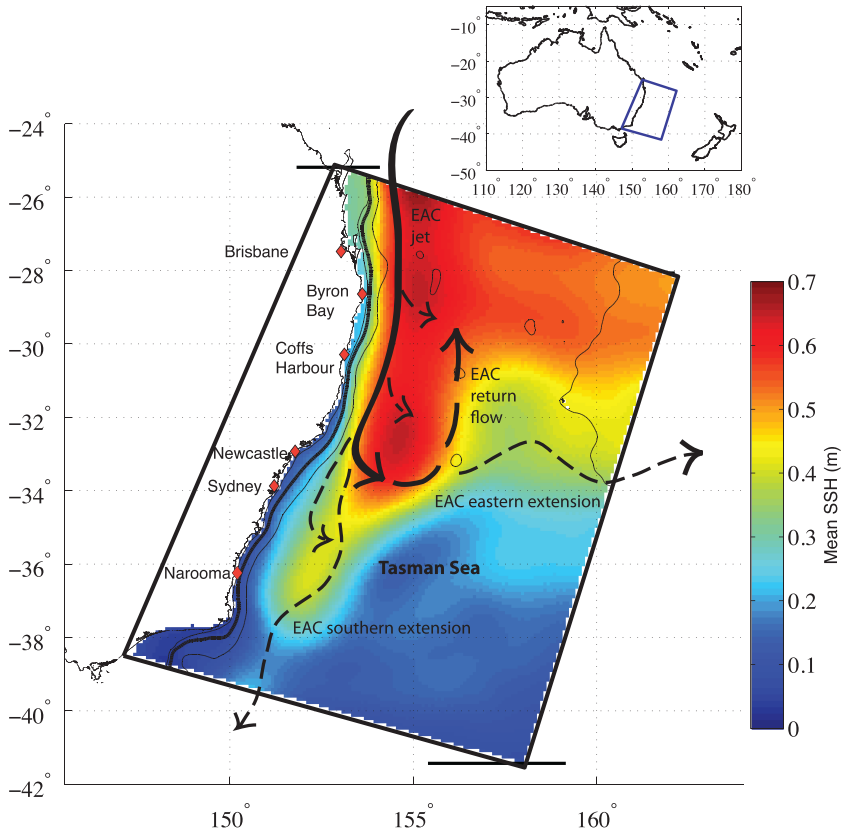

Figure 1. Model domain showing mean SSH from 22-year model simulation and schematic of the EAC System adapted from Oke, Roughan, et al. (2019). Black solid lines denote permanent currents and black dashed lines denote transient currents associated with "eddy trains." Model bathymetry contours at 100 m, 200 m (bold), and 2,000 m are shown. Towns are shown by the red diamonds.

been described that may cause the EAC to separate from the coast and generate eddies in the Tasman Sea, including intrinsic instabilities in the EAC jet, the westward propagation of Rossby waves from the Tasman Sea, changes in along-shelf bathymetry and coastline orientation, and surface forcing variability (Bowen et al., 2005; Bull et al., 2017, 2018; Marchesiello & Middleton, 2000; Mata et al., 2006; Tilburg et al., 2001; Wilkin & Zhang, 2007). The considerable variance observed in the EAC at intra-annual frequencies (periods of 90–180 days) relates to the timescale of eddy shedding (Bowen et al., 2005; Mata et al., 2006; Wilkin & Zhang, 2007). Sloyan et al. (2016) show timescales of 60–120 days for the onshore-offshore meander of EAC jet at 27.5° S and Archer et al. (2017) show meandering, core velocity, width, and EKE exhibit dominant variability at 65–100 days at 30° S.

The first description of the annual cycle in the EAC was provided by Ridgway and Godfrey (1997) using steric heights derived from in situ observations. They showed stronger poleward EAC flow in summer with a seasonal amplitude of up to 6 Sv. Cetina Heredia et al. (2014) show significant annual variability of the poleward transport between 28° S and 34° S and Schaeffer et al. (2014) show an annual signal in the cross-shelf transport related to the along-shelf geostrophic current off Coffs Harbour (30° S) and Sydney (34° S). The stronger EAC flow in summer is associated with higher EKE in the Tasman Sea (Qiu & Chen, 2004) and a poleward shift in the separation latitude (Ypma et al., 2016). Using observations of surface velocities over a 100-km square area upstream of the EAC separation point, Archer et al. (2017) show seasonality in the EAC core velocity and eddy kinetic energy with a maximum mean magnitude and variance in summer and minimum in winter.

Much progress has been made in our understanding of the EAC and EAC eddies through both modeling (e.g., Bull et al., 2017, 2018; Marchesiello & Middleton, 2000; Tilburg et al., 2001; Wilkin & Zhang, 2007; Ypma et al., 2016) and observational (e.g., Archer et al., 2017; Mata et al., 2000; Sloyan et al., 2016; Zilberman et al., 2014; Zilberman et al., 2018) studies, as summarized in Oke, Roughan, et al. (2019), yet several

knowledge gaps remain. Systematic process studies as have been undertaken in the Gulf Stream, Kuroshio, and Agulhas currents have not been carried out in the EAC. Various studies have described the EAC at specific latitudes or studied specific processes; however, differences in observation types, study methodologies, and objectives mean that an overall understanding of the system and of the current's spatial and temporal evolution is missing. We know little about the depth, breadth and strength of the EAC and how it varies with latitude. The mechanisms for the seasonal variability in the strength of the EAC remain unclear. We still do not fully understand the mechanisms driving EAC separation or the factors that influence the instabilities responsible for eddy generation. To answer these questions, we must first gain a thorough understanding of the current's alongshore evolution and its variability at seasonal (annual) and mesoscale eddy related (intra-annual) timescales.

This study presents a comprehensive three-dimensional high-resolution overview of the variability of the EAC system at annual and intra-annual timescales. We have developed a long (22-year) hydrodynamic model simulation that accurately represents the mean EAC path, its separation, its seasonal- and eddy-variability, and its subsurface properties. The model was configured at 2.5- to 6-km horizontal resolution to adequately resolve southeastern Australia's narrow continental shelf, permitting accurate representation of the EAC core as it flows along the shelf break and interacts with the shelf. Using the model, we characterize the temporal (seasonal and intra-annual) and latitudinal variability of flows in the EAC system.

In section 2, we describe the numerical model configuration, and in section 3, we present a detailed validation of the 22-year free-running simulation to provide confidence that the model correctly represents the region's circulation dynamics. Section 4 provides a broad characterization of the flow in the EAC system, presenting mean cross sections of the flow and a volume transport budget. In section 5, we describe the temporal variability of the EAC alongshore transport, its separation, and associated eddy field. In section 6, we describe the alongshore evolution of the current and its seasonal cycle. Section 7 presents the propagating modes of the EAC current core and SSH variability at mesoscale eddy related frequencies. A discussion of the results is provided in section 8.

2. The Regional Ocean Modeling System Configuration

We simulate the atmospherically forced eddying general circulation in the southeastern Australia oceanic region using the Regional Ocean Modeling System (ROMS). ROMS is a free-surface, hydrostatic, primitive equation ocean model solved on a curvilinear grid with a terrain-following vertical coordinate system and a split-explicit time-stepping scheme (Shchepetkin & McWilliams, 2005). The ROMS computational kernel is further described in Shchepetkin & McWilliams (1998, 2003).

The model configuration is the same as that described in Kerry et al. (2016, 2018). The model's northern boundary is at Fraser Island (25.3° S), to the north (upstream) of where the EAC is most coherent at 27.5° S (Sloyan et al., 2016). The domain extends south of the NSW/Victoria border to the latitude of 38.5° S at the coast and approximately 987-km offshore (Figure 1). The model grid is rotated 20° clockwise to be orientated in the alongshore and cross-shore directions.

The model is configured with 30 vertical s-layers distributed with a higher resolution in the upper 500 m and near the bottom, using the vertical stretching scheme developed by De Souza et al. (2015). At a chosen grid cell where the model is 4,000 m deep, there are 12 vertical layers in the upper 100 m ranging from 3.5 m thickness at the surface to 17 m, and there are 20 layers in the upper 500 m. At a 400-m-deep grid cell, there are 19 layers in the upper 100 m ranging from 2 m thickness at the surface to 11 m, the maximum layer thickness is 40 m at 290 m depth, and the bottom layer is 18 m thick. The model's maximum depth is 4,942 m. The bathymetry for the model was obtained from the 50-m Multibeam Dataset for Australia from Geoscience Australia (Whiteway, 2009).

The model has a variable horizontal resolution in the cross-shore direction, with 2.5 km over the continental shelf and slope gradually increasing to 6 km offshore. The horizontal resolution is 5 km in the alongshore direction. The variable cross-shore resolution allows improved bathymetric resolution over the continental shelf and minimizes horizontal pressure gradient (HPG) errors (Haidvogel et al., 2000; Haney, 1991; Mellor et al., 1994) over the steep topography of the continental slope, while reducing computational expense by allowing coarser resolution in the deep ocean. For this study, HPG errors were reduced to an acceptable level using a smoothing method in which a high priority was placed on maintaining the width of the continental

shelf and preserving the seamounts that potentially play a role in steering of the EAC. Accurate representation of the continental shelf was paramount as the narrowing of the shelf is thought to play a key role in EAC separation (Oke & Middleton, 2000).

The model simulation is performed over an approximately 22-year period, from 1 January 1994 to 1 October 2016. The model uses initial conditions and boundary forcing from the CSIRO's BlueLink Reanalysis (BRAN3p5) (Oke et al., 2008, 2012), and this time period is chosen as it covers the entire period over which BRAN3p5 data are available. The boundary forcing is applied daily. Atmospheric forcing is provided by the National Center for Environmental Prediction's (NCEP) reanalysis atmospheric model that has a horizontal resolution of 2.5° by 2.5° (Kistler et al., 2001). The atmospheric forcing fields are specified every 6 hr and used to compute the surface wind stress and surface net heat and freshwater fluxes using the bulk flux parameterization of Fairall et al. (1996). A correction was applied to the surface heat flux forcing such that the SST from the initial conditions and boundary forcing is in balance with the surface forcing for each month. Daily-averaged model fields are saved over the 22-year simulation.

Vertical turbulent mixing of momentum and tracers is parameterized using the Mellor and Yamada (1982) level-2.5, second-moment turbulence closure scheme (MY2.5). At the northern and eastern boundaries, the Chapman condition (Chapman, 1985) is applied to the free surface at the boundaries and the Flather condition (Flather, 1976) is applied to the barotropic velocity so that barotropic energy is transmitted out of the domain. The southern boundary is clamped to the BRAN3p5 boundary conditions. Baroclinic energy is absorbed at the boundaries using a flow relaxation scheme involving a sponge layer over which viscosity and diffusivity are increased linearly by a factor of 10 from the values applied within the model domain for the northern and eastern boundaries, and a factor of 20 for the southern boundary. The clamped southern boundary and increased sponge layer were required to give accurate representation of the eddy variability south of the separation zone and ensure the transmission of eddy energy out of the southern boundary of the domain. As shown in the section below, the separation of the EAC from the coast and the eddy variability in the Tasman Sea are well represented in the model, indicating that the circulation pathways in the Tasman Sea are well represented.

3. Model Validation

Free-running ocean models (without data assimilation) are not able to reproduce the temporal evolution of the mesoscale eddies exactly; however, of importance for this study is that the 22-year model simulation reproduces the mean properties of the ocean state and its variability well. As we are interested in annual and intra-annual variability, we focus on accurate representation of the seasonal cycle and the mesoscale eddy related variability. Accurate representation of the depth structure of the EAC is important for this study and comparisons to subsurface observations, climatology, and inferred flow structures from the literature are presented.

To validate the model's representation of SSH variability, we use data from the Archiving, Validation, and Interpretation of Satellite Oceanographic Data (AVISO) product (CNES, 2015). The AVISO product provides global, daily, gridded (1/4° × 1/4°) mean sea level anomaly (SLA) data produced by merging of all available along-track satellite altimetry data, computed with respect to a 7-year mean. The data provide a daily statistical field giving a synoptic view of the SSH. Sampling the model at the same times and locations as the data, we compute the root mean squared (RMS) SSH anomaly from the data and the model (Figures 2a and 2b, respectively). Overall, the shape of the region of enhanced SSH variability is reasonably well represented in the model compared to satellite-derived SSH data from AVISO over the 22-year period. Because the SSH variability is dominated by mesoscale eddy activity, this validation indicates that the model accurately describes eddy variability. The difference in RMS SSH anomaly (modeled minus observed) is shown in Figure 2c, with the model slightly underestimating the mesoscale SSH variability along the EAC eastern extension and slightly overestimating the variability in the north eastern Tasman Sea and south of the EAC separation zone.

The latitudes at which the EAC separates from the coast are computed from daily-averaged surface fields of velocities and SSH from the model and from geostrophic velocities and SSH fields from AVISO. To compute the separation latitudes, we follow the method used by Cetina Heredia et al. (2014). We find the highest poleward velocity through the cross-shore section off 27.5° S (where the EAC is most coherent, Sloyan et al., 2016) and follow the corresponding SSH contour. The separation latitude is defined as the latitude at which

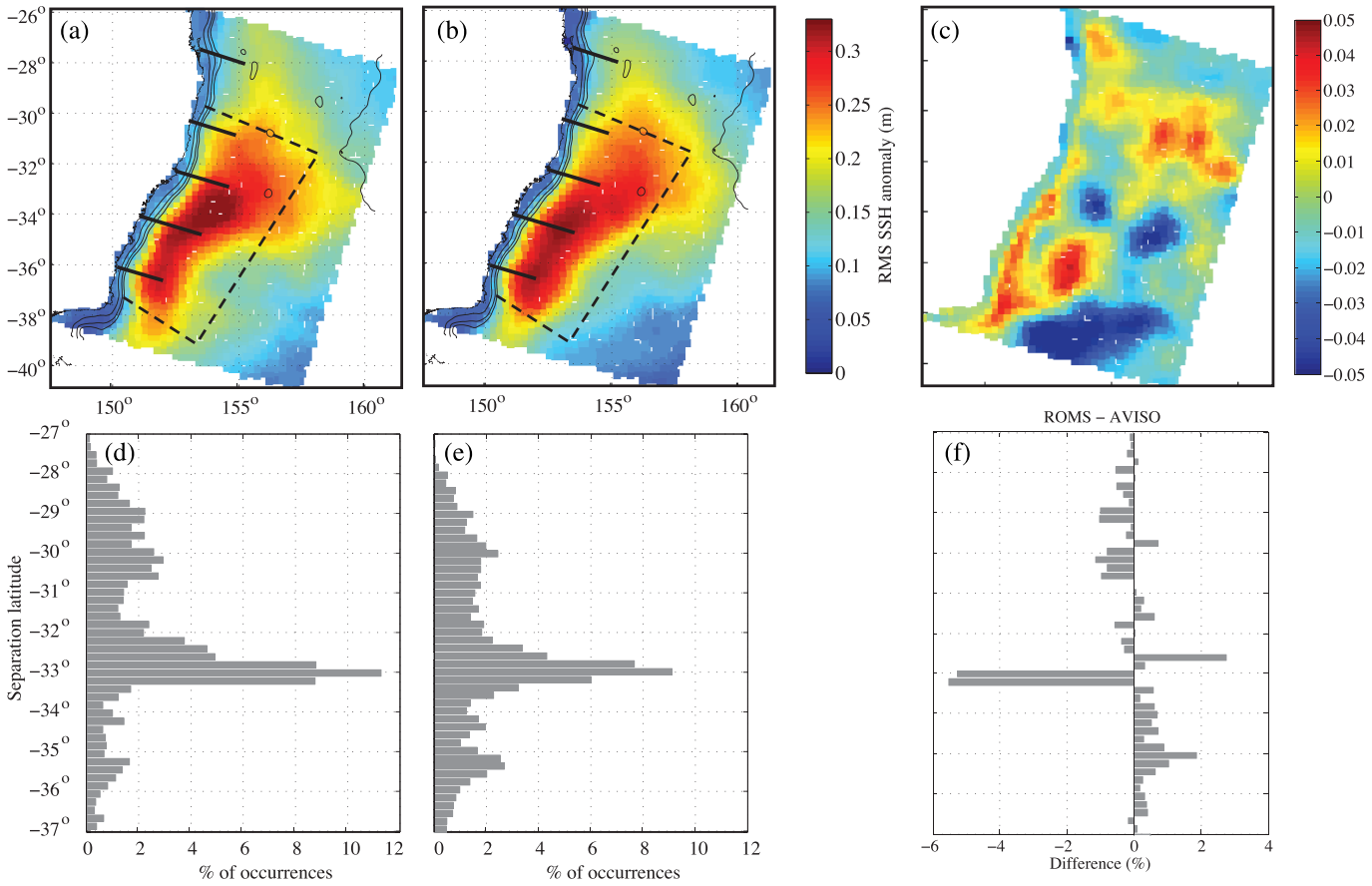

Figure 2. Root mean squared SSH anomaly over 22-year period from (a) AVISO and (b) ROMS. Cross-shore sections for transport calculations are shown by the black lines, and the area over which EKE is computed is shown by the black dashed lines. The 100-, 200-, and 2,000-m bathymetry contours are shown. The difference between (b) and (a) is plotted in (c). Percentage occurrence of EAC separation with latitude for (d) AVISO and (e) ROMS. Plots include all separations including after reattachment. The difference between (e) and (d) is plotted in (f).

the SSH contour detaches by more than 70 km offshore of the 150-m bathymetry contour. The EAC can reattach and separate several times for a single surface field snapshot. The model provides a good representation of the EAC separation, with both model (Figure 2d) and data (Figure 2e) showing a peak at ~ 30° S, the highest occurrence of separation between 32° S and 33.5° S, and another peak at ~ 35.5° S. The difference plot (modeled minus observed, Figure 2f) shows the model has more separation instances just north of 33° S than as inferred from AVISO data, underestimates separation just south of 33° S and slightly overestimates separation south of the main separation zone. In the model, the EAC sheds eddies on average every 100 days, consistent with the eddy shedding period in the OCCAM (Ocean Circulation and Climate Advanced Modeling Project) global ocean model (Saunders et al., 1999) and the eddy shedding period computed by Mata et al. (2006) from satellite altimetric observations.

To validate the model's representation of sea surface temperature (SST), we use SST observations from the SRS Satellite Level 3 one-day composite data obtained though Australia's Integrated Marine Observing System (IMOS; https://portal.aodn.org.au). This is a multisensor SST skin product providing a nighttime observation, derived using data from AVHRR instruments on all available NOAA polar-orbiting satellites and provided with 0.02° × 0.02° resolution. Timeseries of the daily domain-averaged SST from the observations and the model sampled at the observation locations show good agreement in the SST seasonal cycle, seen by comparing the harmonic fit to the annual cycles of these timeseries. For the observations, the SST seasonal cycle has an amplitude of 2.49° C and a phase of 54.53° about a mean of 20.67° C. For the model, the amplitude is 2.39° C with a phase of 56.66° about a mean of 20.97° C. The residuals are normally distributed for both model and observations, and the RMS of the residuals between the spatially averaged data and their seasonal fit is 1.17° C for the observations and 1.00° C for the model.

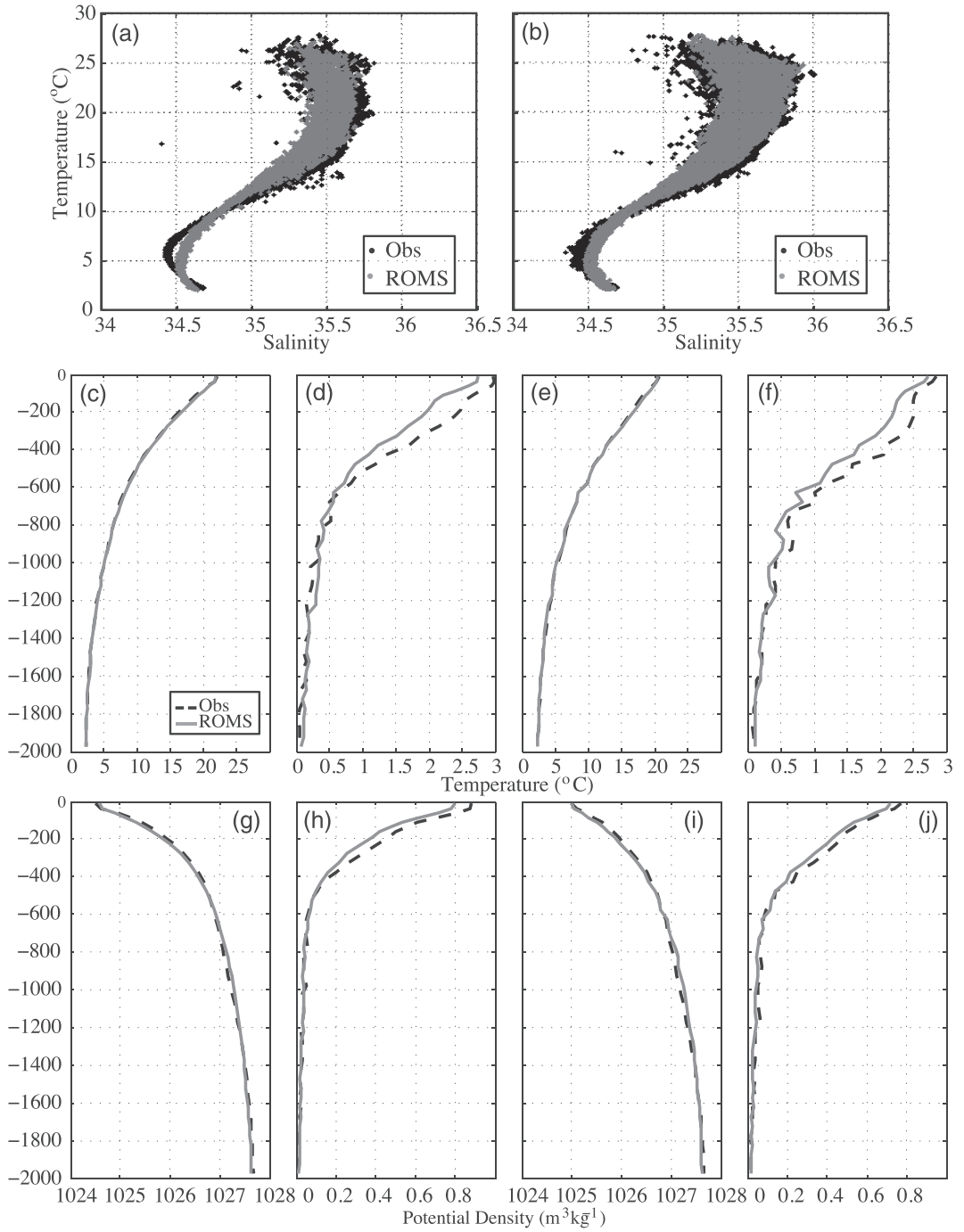

Figure 3. T-S diagram for the Argo observations and ROMS model sampled at Argo observation times and locations, for Argo profiles taken over (a) the continental slope, and (b) offshore. Mean temperature and RMS anomaly of temperature for Argo observations and the corresponding values from the ROMS model for Argo profiles taken over the continental slope (c and d, respectively), and for offshore profiles (e and f). Mean potential density and RMS anomaly of potential density for Argo observations and the corresponding values from the ROMS model, for Argo profiles taken over the continental slope (g and h respectively), and for Argo profiles taken offshore (i and j). The observations consist of 5,807 offshore profiles and 324 profiles over the continental slope over the 22-year modeled period.

The applied atmospheric forcing is in balance with the BRAN3p5 boundary conditions; there is no net temperature drift over the 22 years and the time mean spatial SST fields match well between BRAN3p5 and the ROMS model. Offshore of the 1,000 m contour the mean SST difference between BRAN3p5 and ROMS is 0.002° C; however, inshore of 1,000 m the ROMS model is 0.35° C cooler than BRAN on average. This is because the ROMS model resolves the bathymetry of the continental slope and shelf better than its parent model, resolving physical processes such as upwelling.

We make use of data from Argo profiling floats to validate the subsurface representation of the model. Argo is an international program consisting of nearly 4,000 free-drifting profiling floats that measure the temperature and salinity of the upper 2,000 m of the global ocean (www.argo.ucsd.edu, http://doi.org/10.17882/42182). Data in our region are available beginning in November 2002 through to the end of our modeled period (October 2016). For the validation, we extract the modeled values at the observation times and locations and use data only over the modeled period to minimize bias due to spatial inhomogeneity and low-frequency (interannual to decadal) variability. To present validation over the continental slope and offshore, we separate our analysis into Argo profiles taken over the continental slope (of which there are 324) and Argo profiles taken offshore (of which there are 5,807). Figures 3a and 3b show the temperature-salinity (T-S) diagram for the Argo observations and the ROMS model sampled at the Argo observation times and locations over the continental slope and offshore, respectively, showing that the T-S signature of the subsurface waters matches observations from Argo well. Figures 3c and 3e show the mean temperature from the Argo observations and the corresponding values from the ROMS model computed in depth bins, every 25 to 200 m depth and every 50 m below that, for Argo observations taken over the continental slope and offshore, respectively. The mean potential density profiles, computed using the temperature and salinity observations from Argo floats and their corresponding modeled values, are shown in Figures 3g and 3i, for the slope and offshore observations.

The RMS observation anomaly profiles are plotted in Figures 3d and 3f for temperature over the slope and offshore, and Figures 3h and 3j for potential density. The variability profile shapes match reasonably well both over the continental slope and offshore; however, the model slightly underestimates the subsurface variability from 0 to 600 m over the continental slope and 0 to 1,200 m offshore. For temperature, the variability is underestimated by up to 0.4° C with the maximum difference at 400 m, the approximate thermocline depth. The underestimation of subsurface variability in the model may result from errors of representativeness, which can occur due to (1) the temporal and spatial discretization of the model and (2) physical processes that are not resolved by the model and cannot be removed from the observations, such as internal tides and inertial oscillations. Because we use a free-running model, the difference in subsurface variability between the model and observations may also relate to the Argo floats sampling different ocean features in the model and the observations.

The temperature depth structure across the EAC represented by the 22-year ROMS simulation is compared to climatology by comparing mean temperature cross sections from the model and the Commonwealth Scientific and Industrial Research Organisation (CSIRO) Atlas of Regional Seas climatology (CARS, Ridgway et al., 2002) for the five cross-shore sections shown in Figure 2. CARS climatology is created by averaging and interpolating all available oceanographic profile data, most of which was collected in the last 50 years. Both the model and CARS climatology reveal an upslope thermocline tilt (Figure 4) associated with the southward flowing EAC. The model shows a warm bias that reaches up to 1° C over the core of the EAC for the Brisbane and Coffs Harbour sections (Figures 4a and 4b, right panels) and up to 1–1.5° C over the Forster, Sydney, and Narooma sections (Figures 4c–4e, right panels). This warm bias may be due to the CARS data covering a longer and earlier averaging period and being mapped at a much coarser horizontal resolution (0.5°). Differences over the continental shelf and slope are expected as these regions are not well resolved by CARS.

The mean EAC alongshore flow structure was inferred from XBT, Argo, and altimeter data at the nominal PX30 transect (26–27° S) over the 2004–2015 period by Zilberman et al. (2018). Sloyan et al. (2016) present an 18-month EAC alongshore velocity mean computed from the EAC array velocity observations at 27.5° S. The flow structures presented by Zilberman et al. (2018) and Sloyan et al. (2016) are compared to the modeled mean section at 27.5° S (Figure 4a, left panel). The 0.5 ms^{-1} poleward velocity contour extends to a similar depth (155–170 m) for the modeled mean section, the section inferred by Zilberman et al. (2018) and the section presented by Sloyan et al. (2016). The 0.2 ms^{-1} contour extends to about 400 m the modeled

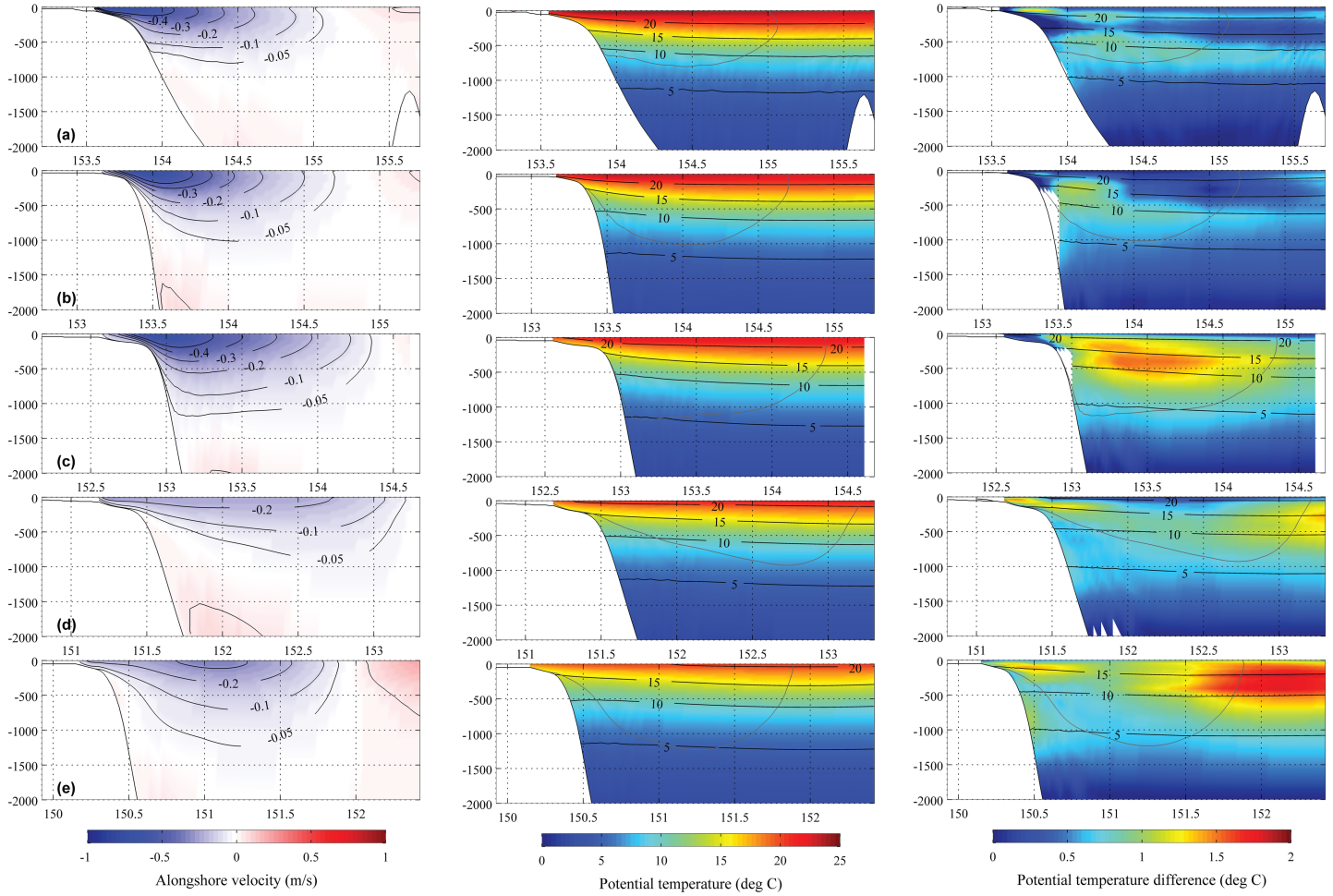

Figure 4. Left column: Mean alongshore velocity from the ROMS 22-year simulation, Middle column: mean temperature from the ROMS simulation, and Right column: difference between model mean temperature and mean temperature from CARS climatology, for the cross-shore sections that cross the coast at Brisbane (27.5° S, a), Coffs Harbour (30.3° S, b), Forster (32.3° S, c), Sydney (33.9° S, d), and Narooma (36.2° S, e). Sections are shown in Figures 2a and 2b. The -0.05 ms^{-1} mean modeled alongshore velocity contour is shown on the temperature and temperature difference plots to indicate the mean position of the EAC.

mean and the Zilberman et al. (2018) and Sloyan et al. (2016) sections. The 0.05 ms^{-1} poleward velocity contour from the modeled mean section extends to 800 m, compared to 600 m for the section inferred by Zilberman et al. (2018), while the 0.05 ms^{-1} poleward velocity contour extends below 1,000 m the section presented by Sloyan et al. (2016). In both the modeled mean and the Zilberman et al. (2018) section, the 0.05 ms^{-1} poleward velocity contour extends out to 155° E. The return flow is evident from 155.5° E to 157° E in both and the 0.05 ms^{-1} equator-ward velocity contour extends to a depth of 330 m the model and 250 m the section presented by Zilberman et al. (2018).

At 30° S, Mata et al. (2000) use velocity observations from a mooring array from 1991 to 1994 to present a mean meridional velocity section. Their 0.2 ms^{-1} contour is 500 m deep at 153.8° E compared to 450 m the modeled mean alongshore velocity at 30° S (Figure 4b, left panel). The modeled mean 0.05 ms^{-1} poleward velocity contour has a maximum depth of 1,100 m at 154.1° E, while the 0.05 ms^{-1} poleward velocity contour in Mata et al. (2000) is not closed and has a depth of 1300 m at 154.1° E. Overall, the modeled mean EAC velocity depth structure is in good agreement with the depth structure inferred from observations at both ~ 27° S and ~ 30° S, considering the different averaging periods and the slightly different locations.

From the model, we compute the EAC transport for five cross sections (shown in Figures 2a and 2b) over the cross-sectional area inside the -0.05 ms^{-1} contour in the alongshore velocity mean (as in Kerry et al., 2018). We consider this to be the most appropriate area over which to compute the transport, as it defines the cross-sectional region through which the main EAC jet flows, rather than choosing an arbitrary depth or

Table 1
Alongshore Transport (Sv) Through Cross-Shore Sections (Shown in in Figure 2) Computed Daily for the 22-Year Simulation

	27.5° S	30.3° S	32.3° S	33.9° S	36.2° S
Inside 0.05 ms^{-1} contour					
Mean (Sv)	−18.87	−19.60	−26.76	−14.04	−17.05
Stdev (Sv)	11.57	15.63	20.89	18.53	19.85
Min (Sv)	−56.74	−62.02	−68.33	−56.76	−61.71
Max (Sv)	18.71	30.69	44.11	34.54	28.31
Seasonal Cycle amp. (Sv)	3.88	5.52	5.40	3.09	2.66
Seasonal Cycle pha. (°)	146	163	209	163	72
Area (km^2)	97.1	104.2	141.3	114.5	132.3
Distance offshore (km)	157.6	156.1	178.7	198.7	165.0
Depth (m)	820	1010	1190	980	1250

Note. Transport is computed over the cross-sectional area inside the −0.05 ms^{-1} contour in the alongshore velocity mean. Area, distance offshore and depth correspond to this cross-sectional area. The transport is defined as positive (negative) equatorward (poleward).

computing the transport over the full depth (which has be done previously). The mean, standard deviation, and minimum and maximum alongshore volume transport are shown in Table 1, computed from the daily transports over the 22-year simulation. The transport values are compared to values presented in the literature for the Brisbane and Coffs Harbour sections here. Further analysis of the EAC transport is presented in section 7.

Sloyan et al. (2016) compute volume transport in the EAC from a full-depth mooring array that spans the current at 27.5° S out to 155.3° E over an 18-month period in 2012–2013. They compute a mean net transport above 2,000 m (an arbitrary choice given that they show the level of no motion to be 1,200 m) of −15.8 Sv with a standard deviation of 10.5 Sv. Zilberman et al. (2018) use a combination of XBT, Argo, and altimetry data to estimate a mean poleward alongshore EAC transport from 2004 to 2015 of 19.5 Sv. These estimates are consistent with our values constrained within the −0.05 ms^{-1} contour (which extends to a depth of 800 m; Figure 5a) of −18.87 Sv and a standard deviation of 11.57 Sv. Mata et al. (2000) computed transport from a mooring array located at 30° S, from the coast extending offshore to 154.4° E between September 1991 and March 1994. They find a mean total full-depth transport of 22.1 Sv southward with an root mean squared (rms) variability of 30 Sv. From the 22-year simulation, we compute a full-depth mean net alongshore transport for a section at 30.3° S out to 154.47° E of 13.93 Sv poleward and a standard deviation of 36.15 Sv (not shown in Table 1), and mean net alongshore transport inside the −0.05 ms^{-1} contour (which extends to 1000 m depth; Figure 5b) of −19.60 Sv with a standard deviation of 15.63 Sv. A thorough comparison of EAC transport estimates from observational and modeling studies is given in Oke, Roughan, et al. (2019); however, true comparison is challenging as the estimates differ in the period over which they are calculated, in latitude and in choice of cross-sectional area over which the computation is performed (distance offshore and depth extent).

Overall, we have shown that the 22-year ROMS model simulation provides an accurate representation of the mean dynamical features of the EAC and represents both the surface and subsurface (0–2,000 m) variability well. We find that the model accurately represents the spatial patterns of mesoscale SSH variability and EAC separation, so we are confident that the circulation pathways in the Tasman Sea are well represented. The seasonal SST variability is reproduced by the model and the mean and variability of the subsurface properties are well represented. We now make use of the 22-year model simulation to investigate annual and intra-annual variability in the EAC system.

4. Characterizing Flow in the EAC System

We begin by broadly characterizing the flows across the EAC system. For this purpose, we define five cross-shore sections which extend from 27.5° S, where the EAC is most coherent, to 36.2° S, at which the percentage occurrence of EAC separation falls below 1%, and offshore a distance of 744 km. The five sections

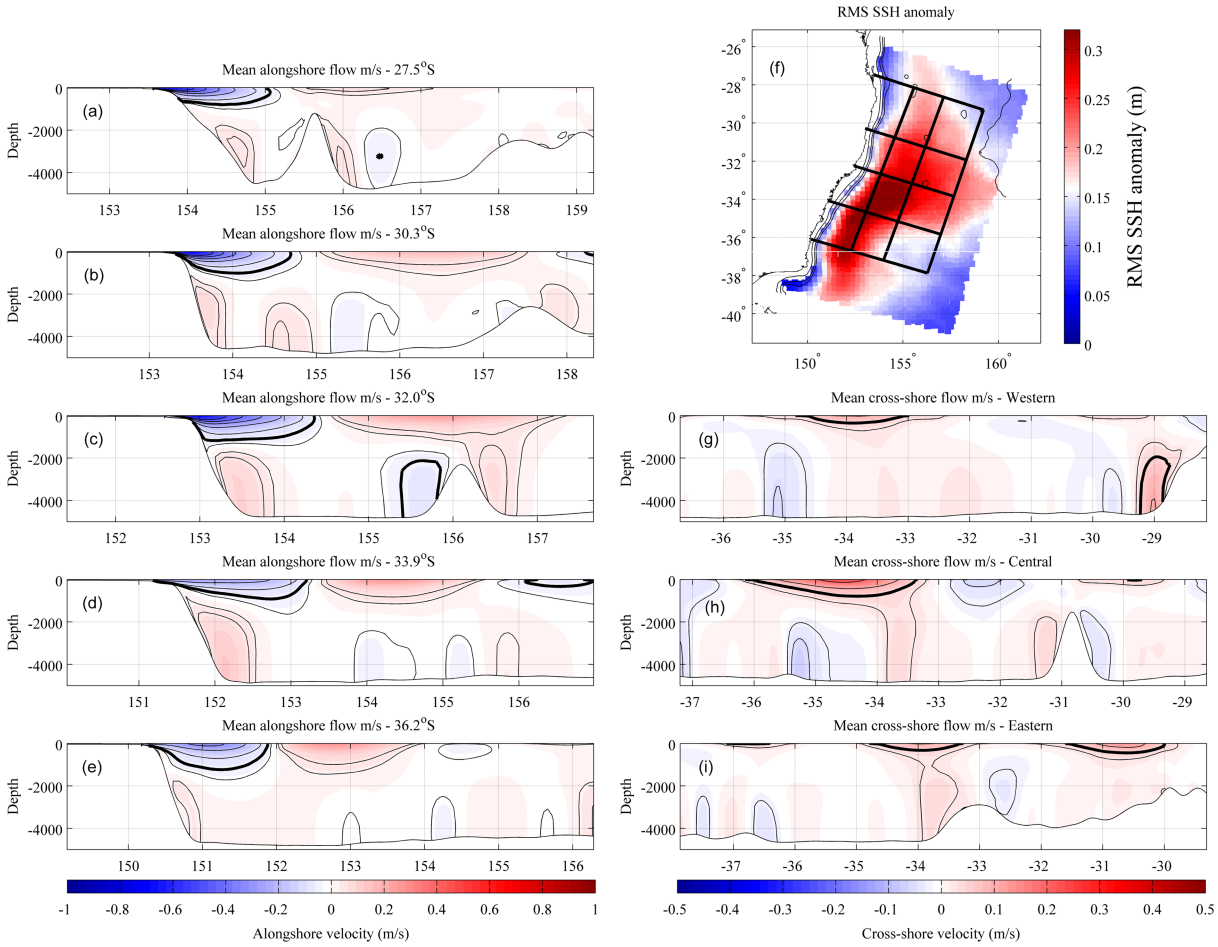

Figure 5. Mean alongshore (a–e) and cross-shore (g–i) velocity sections from 22-year ROMS simulation. The −0.5, −0.4, −0.3, −0.2, −0.1, −0.05(*bold*), −0.025, 0.025 and 0.05 ms^{-1} velocity contours are shown. Sections are overlain on RMS SSH anomaly from 22-years of AVISO observations (f). Note that the velocity scale is different for the alongshore and cross-shore velocity sections.

are chosen to represent (1) where the EAC is most coherent (Brisbane, 27.5° S), (2) north of the typical separation latitude range (Coffs Harbour, 30.3° S), (3) close to the typical separation latitude (Forster, 32.3° S), (4) south of the typical separation region (Sydney, 33.9° S), and (5) representative of the EAC southern extension (Narooma, 36.2° S). In the alongshore direction, we define three sections that join the northern and southern most cross-shore sections and are 989 km in length. These sections are shown by the black lines in Figure 5f overlain on the RMS SSH anomaly.

4.1. Mean Flow Sections

The alongshore and cross-shore flow structure can be seen in Figure 5, which shows the mean alongshore flow through the five cross-shore sections (Figures 5a–5e) and the mean cross-shore flow through the three alongshore sections (Figures 5g–5i). For this study we define the mean EAC core as the area within the −0.05 ms^{-1} contour in the mean alongshore velocity for the cross-shore sections (and the 0.05 ms^{-1} contour in the mean offshore velocity for the alongshore sections). From 27.5° S to 32.0° S, the poleward flow in the EAC jet intensifies and the mean jet broadens and deepens from a depth of 800 m and width of 160 km at 27.5° S to a depth of 1200 m and width of 180 km at 32° S. Separation occurs between 31° S and 34° S 50% of the time and between 32.0° S and 33.5° S (referred to hereafter as the typical separation region) 38% of the time (Figure 2d). At 34° S, the mean poleward flow is weaker, shallower (1,000 m), and broader (200 km) than at 32° S. Return flow of the EAC offshore of the poleward current occurs at all five sections, with the feature being broadest at 32° S (Figure 5c) consistent with the schematic overlain on the SSH mean in Figure 1. The downstream evolution of the EAC core and its associated alongshore transport is presented in detail in section 6.1.

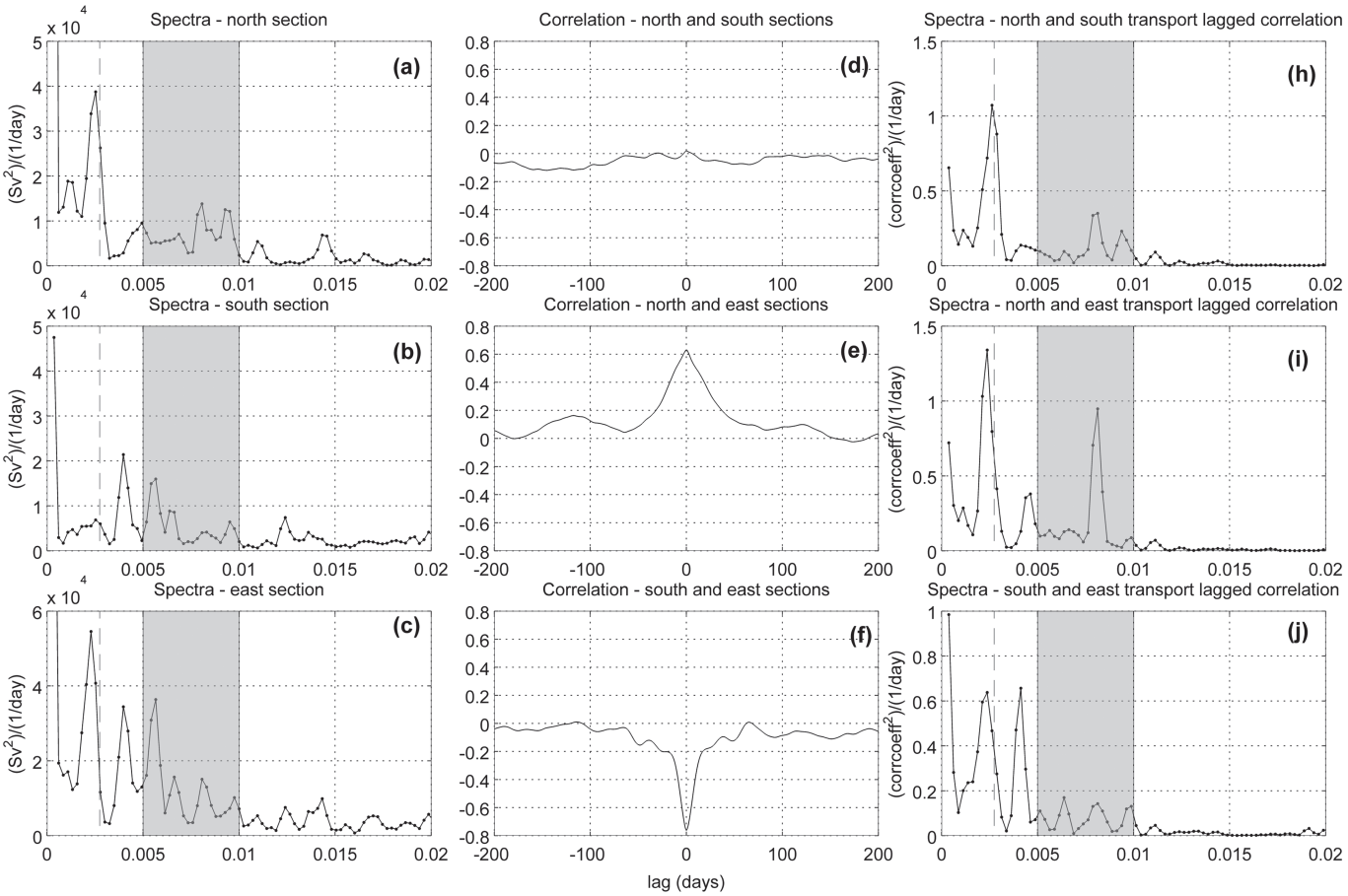

Figure 6. Spectra of full-depth transport through the (a) north, (b) south, and (c) east sections from 22-year ROMS simulation (sections are shown in Figure 5). Lagged correlation between transport through the (d) north and south sections, (e) north and east section, and (f) south and east sections. Spectra of the lagged correlation between transport through the (h) north and south sections, (i) north and east sections, and (j) south and east sections. For the spectra, the frequency corresponding to the annual period is shown by the gray dashed line, and the gray shaded areas show the frequency band corresponding to periods of 100–200 days. For the correlations, transport is defined as positive poleward (for the north and south sections) and eastwards (for the east section).

For the alongshore sections, the mean eastward flow is weakest through the western section (that runs adjacent to the poleward flowing core of the EAC jet), intensifies at the central section, and then is weaker again through the eastern section (Figures 5g–5i). The strongest mean flow through the central section (Figure 5h) is centered around 34.5° S corresponding to the most common separation path, as depicted in Figure 1, and to the intersection of the alongshore section and the highest RMS SSH anomaly (Figure 5f). An onshore flow from 32° S to 32.5° S occurs due to recirculation. The offshore flow at the eastern section is concentrated in two jets in the time mean flow fields (Figure 5i) at 30.6° S (480 m deep) and at 34.0° S (320 m deep).

4.2. Inflows and Outflows

The northern, eastern, and southern most sections (Figure 5f) define a box that bounds the EAC system and we compute the total full-depth transport through these boundaries. A time-mean southward transport of 19.5 Sv enters the bounding box through the northern section (with a standard deviation of 10.9 Sv), 12.1 Sv exits through the eastern boundary (with a standard deviation of 16.8 Sv), and 7.4 Sv through the southern boundary (with a standard deviation of 13.1 Sv). Of the poleward flow entering via the EAC jet in the north (Figure 5a), 62% exits the region via the east (Figure 5i) and 38% continues south (Figure 5e).

Frequency spectra of poleward transport through the northern section (Figure 6a) and the EAC eastern extension (Figure 6c) both display peaks at the annual period, with increased energy at higher frequencies (in the intra-annual period range) for the eastern section transport. Transport through the southern section (Figure 6b) does not show a strong spectral peak at the annual period, with most of the energy at periods of 150–250 days.

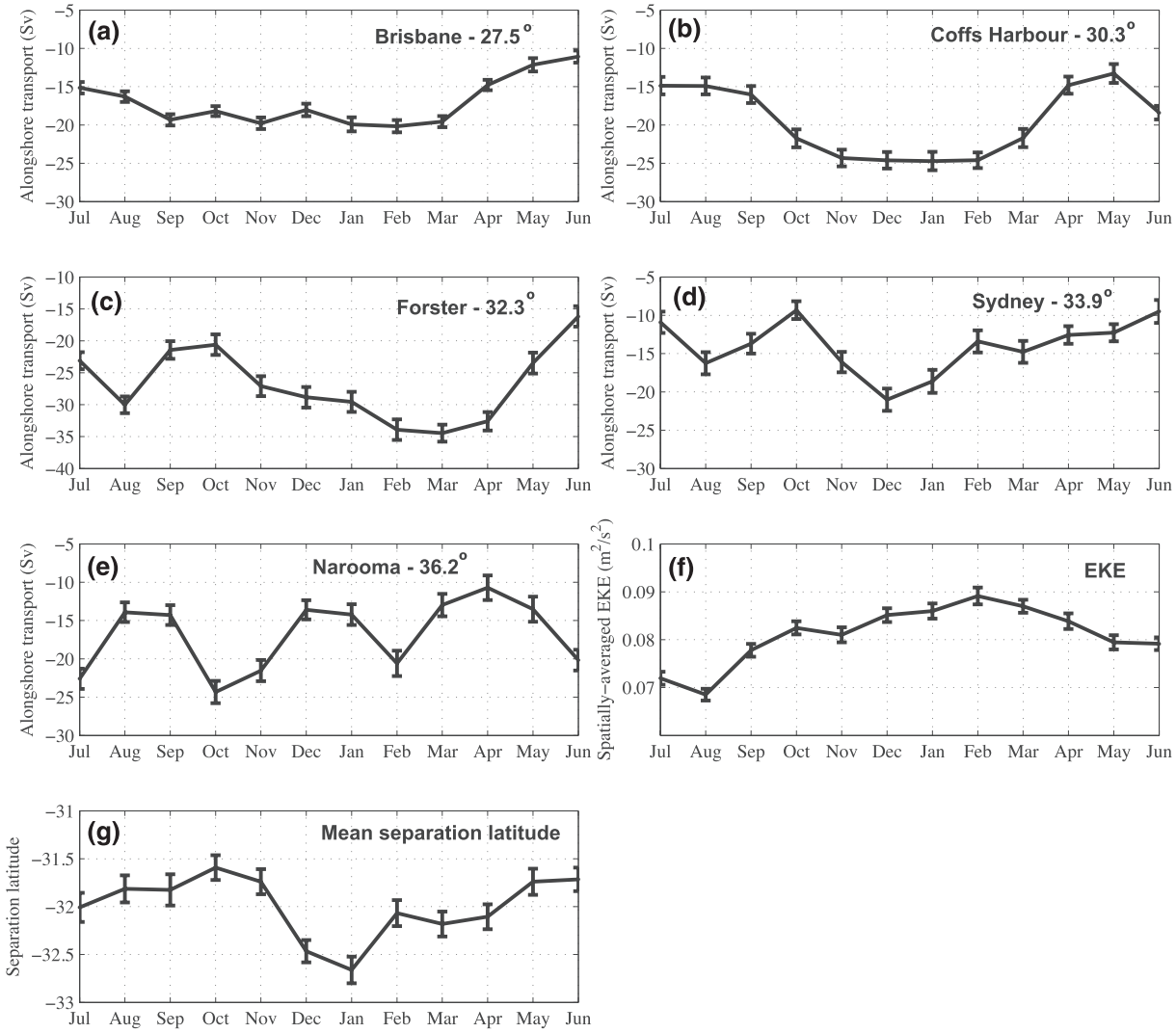

Figure 7. (a–e) Daily-averaged volume transport through the five sections (sections are shown in Figure 2), (f) daily spatially averaged EKE in the upper 450 m(averaging region shown in Figure 2) and (g) daily separation latitude, grouped by month over the 22 years and averaged. Error bars show 95% confidence intervals.

Poleward transport through the northern section is positively correlated with offshore transport in the EAC eastern extension (Figure 6e), with a correlation of 0.6 at zero time-lag and a decorrelation time-scale of 150-180 days. Eastward transport in the EAC eastern extension displays a negative correlation with the poleward transport in the EAC southern extension (Figure 6f), with a correlation coefficient of -0.8 and a time-scale of 70 days to zero correlation. Transport through the north and south sections show weak correlations (< 0.1) (Figure 6d) and the time-lagged correlations vary predominately at annual periods (Figure 6h). The time-lagged correlations between the transport through the northern and eastern sections shows a strong spectral peak at the annual period and a peak at 125 days, which is close to the typical mesoscale eddy shedding period of 100 days (Figure 6i). The time-lagged anticorrelation between the eastern and southern EAC extensions shows two spectral peaks of approximately equal magnitude at the annual period and at 240 days (Figure 6j).

5. Temporal Variability

5.1. Poleward Transport

Poleward transport varies on both seasonal and mesoscale eddy related timescales. We begin by quantifying the mean and variability in alongshore transport from the model through the five cross-shore sections (Figure 5f). We compute the transport over the cross-sectional area inside the -0.05 ms^{-1} contour in the

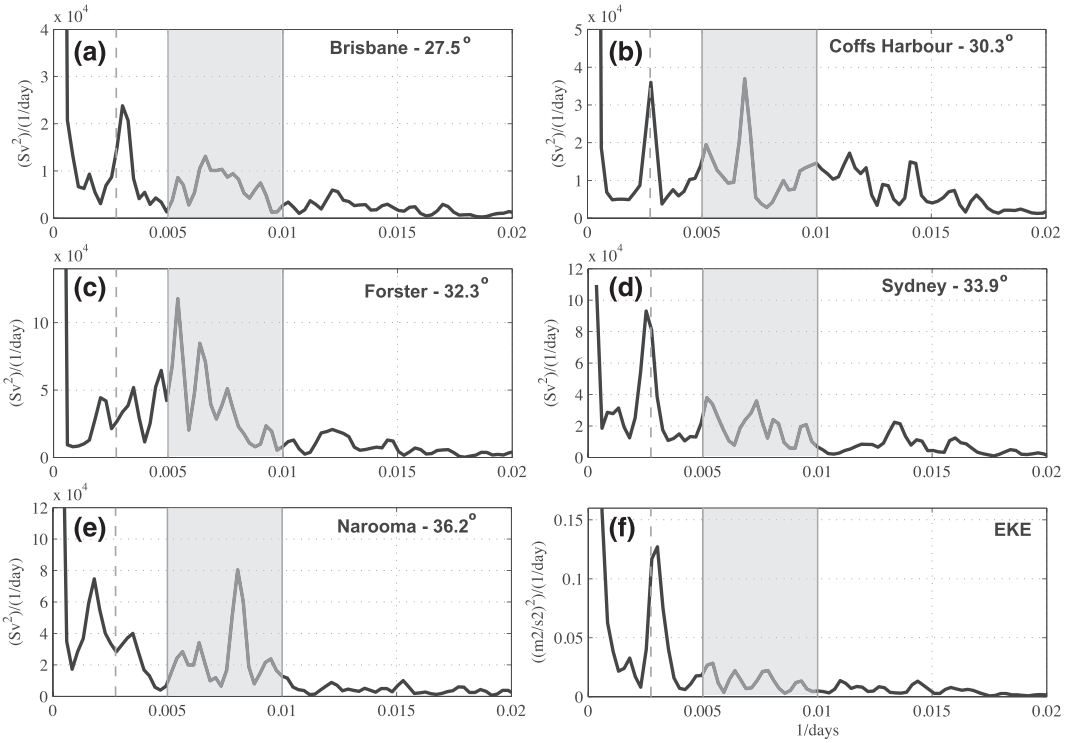

Figure 8. Frequency spectra of (a–e) volume transport through the five sections (sections are shown in Figure 2) and (f) spatially averaged EKE in the upper 450 m (averaging region shown in Figure 2).The frequency corresponding to the annual period is shown by the gray dashed line, and the gray shaded areas show the frequency band corresponding to periods of 100–200 days.

alongshore velocity mean (as in Kerry et al., 2018) so as to define a cross-sectional region through which the main EAC jet flows. The cross sections are shown in Figures 2a and 2b (they are the same latitudinal sections as in Figure 5f but extend only to the offshore extent of the -0.05 ms^{-1} contour). Values of the mean, standard deviation, and minimum and maximum alongshore volume transport through the five sections are shown in Table 1, computed from the daily transports over the 22-year simulation. The offshore distances and cross-section areas are included in Table 1.

Averaging the 22 years of daily alongshore transports for each month of the year conveys the transport seasonality (Figures 7a–7e). Off Brisbane, poleward transport is constant, within the error bars, between September and March. Poleward transport is strongest over the Austral summer for the Coffs Harbour, Forster, and Sydney sections, although transport off Forster shows a lag of approximately 2 months. The phase lags are more clearly seen by computing the transport annual cycle harmonic fit for the five sections (shown in Table 1). The phase difference between the 27.5° S section and the Coffs Harbour section to the south corresponds to a lag of about 2 weeks. Based on the annual cycle harmonic fit, at 27.5° S the EAC has its strongest poleward transport in mid-December and weakest in mid-June, while at 30.3° S (and at 33.9° S) the strongest and weakest occur during late December and late June, respectively. At 32.3° S, the peak occurs about 45 days later, with the strongest poleward transport in mid-February and weakest in mid-August. South of the separation point, at 33.9° S, the phase is the same as that upstream of the separation point. The annual cycle of alongshore transport through the most poleward section (Narooma, 36.2° S) shows a maximum poleward transport occurring late September and a minimum late March, out of phase with the Sydney section by about 3 months. However, this seasonal signal is less clear in Figure 7e, which reveals three peaks with the poleward transport peaking in February, July, and October.

Frequency spectra of the daily alongshore transport through the five sections show strong peaks at the annual period at the Brisbane, Coffs Harbour, and Sydney sections, with elevated energy in the intra-annual (100–200 days) range at all five sections (Figures 8a–8e). Off Brisbane and Sydney, the seasonal peak dominates, while off Coffs Harbour, the spectral peak at 145-day periods is of similar magnitude to the seasonal

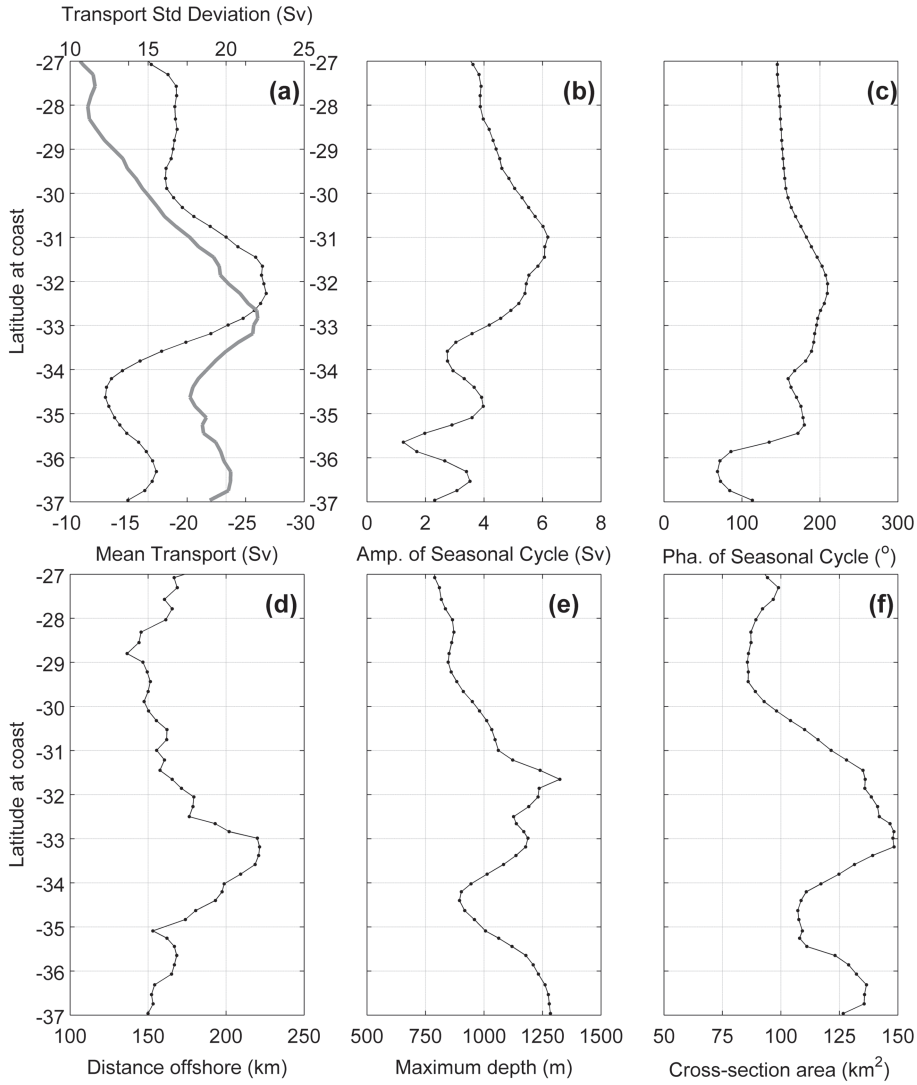

Figure 9. Alongshore transport computed every five model grid cells (~ 25 km) from 22-year ROMS simulation. (a), Mean and standard deviation (gray line) of transport, (b) amplitude of the seasonal cycle harmonic fit, and (c) phase of the seasonal cycle harmonic fit. For alongshore mean transport (computed inside the -0.05 ms^{-1} contour in the alongshore velocity mean), we show (d) the distance offshore, (e) maximum depth, and (f) cross-sectional area. The transport is defined as positive (negative) equatorward (poleward).

peak. The spectral peak in the intra-annual range off Coffs Harbour illustrates the impact of eddy shedding on alongshore transport, which occurs more often here than off Brisbane or Sydney (Figure 2c). Off Forster, within the typical separation latitude range, the frequency spectra contains most energy in the intra-annual scale, with the strongest peak at 184 days. Interestingly, a strong seasonal peak in transport is evident off Sydney, while off Narooma, the strongest peak is in the intra-annual range at 125 days.

5.2. Current Separation and Eddy Variability

When the EAC separates from the coast, eddies form in the Tasman Sea and both the separation latitude and EKE have been shown to display seasonality. From the 22-year model simulation, the separation latitude is computed as described in Section 3 above. Monthly averages of the latitude at which the EAC separates from the coast for the first time show a southward migration by about 1° in January compared to June (Figure 7g), with separation occurring at 31.7° S on average in June and at 32.7° S in January.

On average, the highest EKE in the Tasman Sea occurs in February and the lowest in August (Figure 7f). EKE is computed daily spatially averaged over the region of elevated SSH variability (dashed line in Figures 2a and 2b) and over the upper 450 m. This spatial and depth average is consistent with the metric used in Kerry

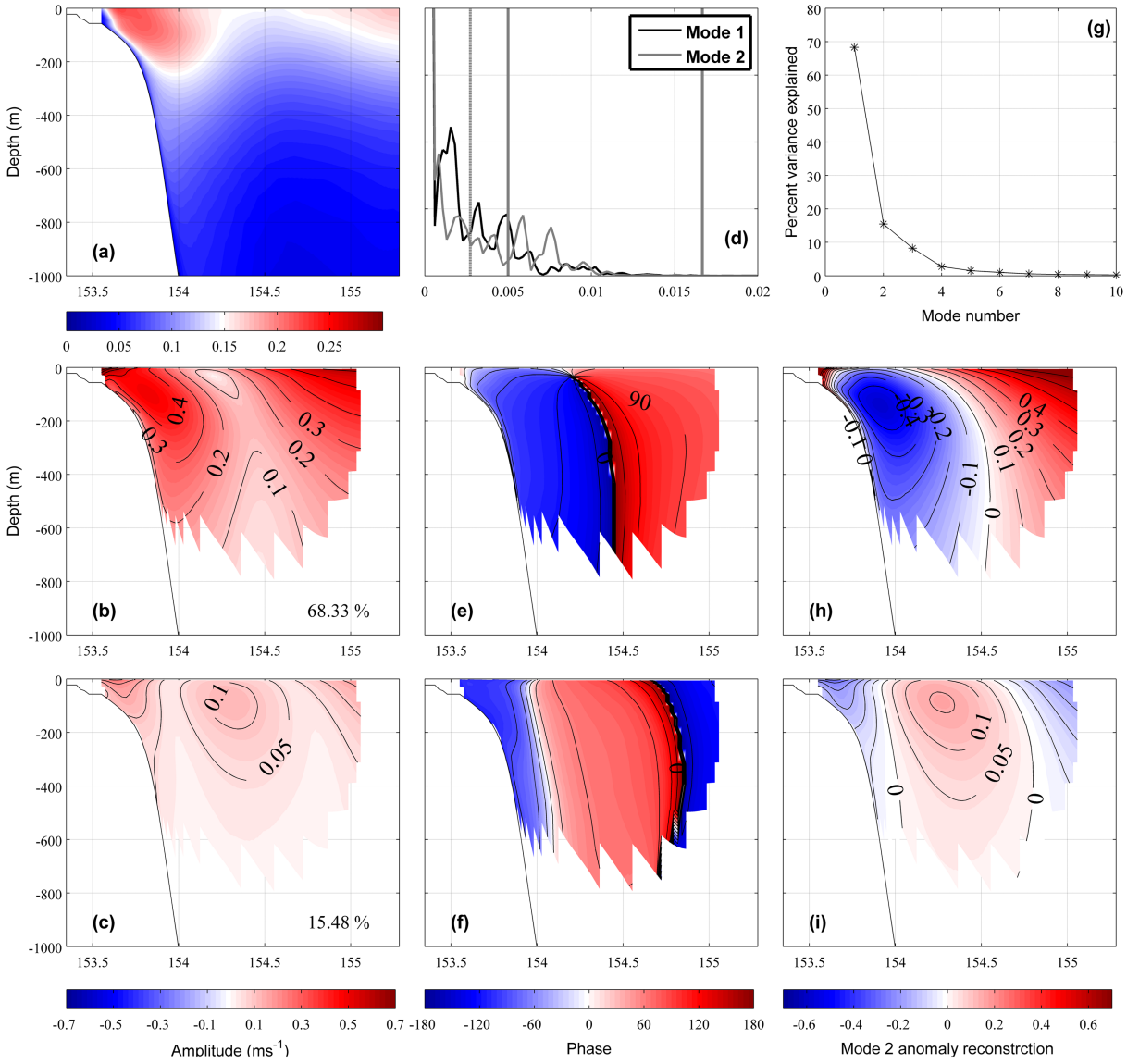

Figure 10. Complex EOFs for alongshore velocity through the 27.5° S cross-section bandpass filtered at 60–200 days. (a) Standard deviation and (d) frequency spectra of the temporal expansion functions of the Mode-1 and Mode-2 CEOFs. The vertical gray lines on (d) show, from left to right, the frequencies corresponding to the annual period, to 200 days and to 60 days. A Scree plot (g) shows the percent variance explained against mode number. (b) Spatial expansion function amplitude of CEOF Mode 1, (e) phase of Mode 1, and (h) Mode-1 anomaly reconstruction. (c) Spatial expansion function amplitude of CEOF Mode 2, (f) phase of Mode 2, and (i) Mode-2 anomaly reconstruction. Percentage variability explained by each mode is printed on the amplitude plots. Spatial expansion functions are scaled such that the temporal expansion functions range between −1 and 1.

et al. (2018) and the upper 450 m was chosen as the EKE is highest in this depth range. A harmonic fit of the annual cycle to the daily spatially averaged EKE time series shows the peak in EKE occurs at the beginning of February, which lags the peak in poleward transport through 27.5° S (which occurs mid-December) by 55 days and the transport through 30.3° S (which peaks late December) by 37 days, and is in phase with the annual cycle of transport through 32.3° S. The amplitude of the spatially averaged EKE annual cycle is 0.008 $m^2\ s^{-2}$, and the difference between the highest and lowest monthly means (Figure 7f) is 0.021 $m^2\ s^{-2}$, with a minimum average EKE of 0.069 $m^2\ s^{-2}$ in August and a maximum of 0.089 $m^2\ s^{-2}$ in February. EKE shows a strong peak in its frequency spectra at annual periods with relatively little energy in the intra-annual range (Figure 8f), indicating that the average eddy energy over the Tasman Sea is not strongly influenced by specific eddy shedding events.

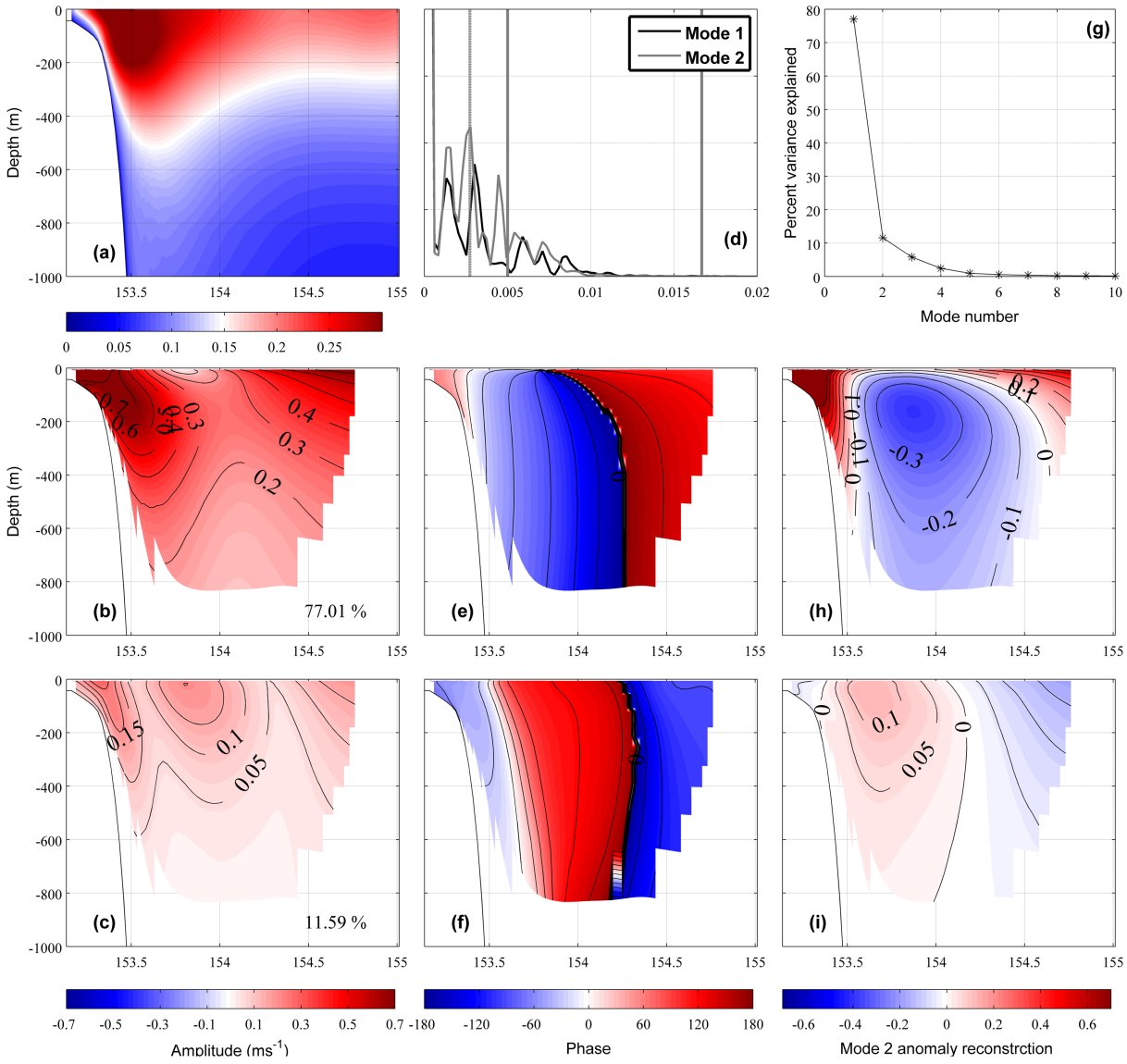

Figure 11. As above for the 30.3° S cross section.

6. Latitudinal Variability

6.1. Poleward Transport and Depth Structure

The description of the flow across the EAC system presented in section 4 and in Figure 5 shows latitudinal variability in the structure of the mean poleward-flowing EAC core. To investigate how the alongshore transport and shape of the EAC core evolves as the current flows poleward, we examine the alongshore EAC flow every 25 km (five model grid cells) from 27° S to 37° S (Figure 9). As above, we compute the transport daily over the cross-sectional area inside the −0.05 ms^{-1} contour in the alongshore velocity mean. Because the mean current section changes as it moves poleward, the distance offshore, maximum depth, and cross-sectional area for the transport computation changes (Figures 9d–9f).

The mean poleward transport is fairly constant from 27.5° S to 30° S (18–19 Sv) then intensifies from 30° S to 32° S reaching 26.8 Sv at 32° S (Figure 9a). The latitudinal range that corresponds to the greatest percentage occurrence of separation (32–33.5° S, Figure 2c) is directly downstream of the peak in mean flow. Poleward of the peak in the mean flow, the standard deviation of EAC transport peaks over the typical separation region, with a maximum value of 22.0 Sv at 32.8° S (Figure 9a). Poleward of the separation region, the mean EAC transport is considerably lower (the weakest mean transport is 13.0 Sv at 34.6° S). The ratio of transport standard deviation relative to the mean poleward transport is considerably greater poleward of the

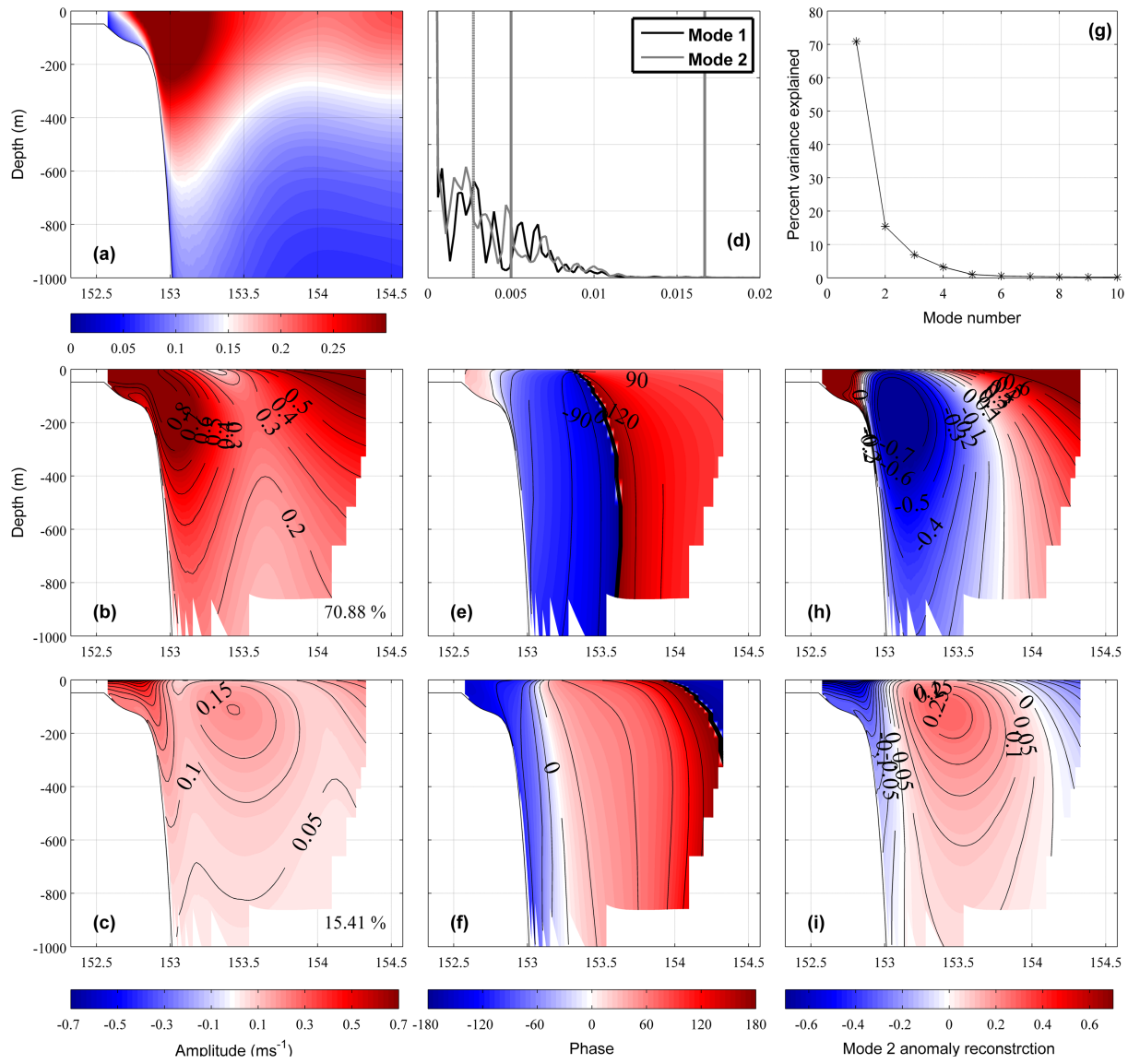

Figure 12. As above for the 32.3° S cross section.

separation latitude (ranging from 0.6 to 0.8 from 27° S to 32° S and 1.1 to 1.4 from 33.5° S to 37° S) indicative of the more eddy-dominated regime.

The depth of the current core is a minimum at 27° S (800 m) and the poleward transport deepens with latitude, to a maximum of 1,300 m at 31.5° S (Figure 9e). The depth of the current is shallower post-separation from 33° S to 34.5° S, and then deepens again from 900 m at 34.5° S to 1,250 m at 37° S. Equatorward of the separation region, the distance that the −0.05 ms^{-1} mean alongshore velocity contour extends offshore is about 150–160 km. The current core broadens over the separation region to a maximum core width of 220 km at 33.1° S (Figure 9d). The current core narrows from 33.1° S to 35° S and south of 35° S the core width is to close to the preseparation magnitude.

6.2. Poleward Transport Seasonal Cycle

The downstream evolution of the alongshore transport seasonal cycle is shown in Figures 9b and 9c. Annual cycle harmonic fits to the 22-year daily transport time series, computed every 25 km (five model grid cells) from 27° S to 37° S, provide seasonal cycle amplitudes and phases. The amplitude of the seasonal cycle (Figure 9b) increases with latitude, from 3.9 Sv at 27.5° S to a maximum of 6.2 Sv at 31° S. Across the typical separation region, the seasonal cycle amplitude decreases from 6.2 to 2.7 Sv at 33.5° S.

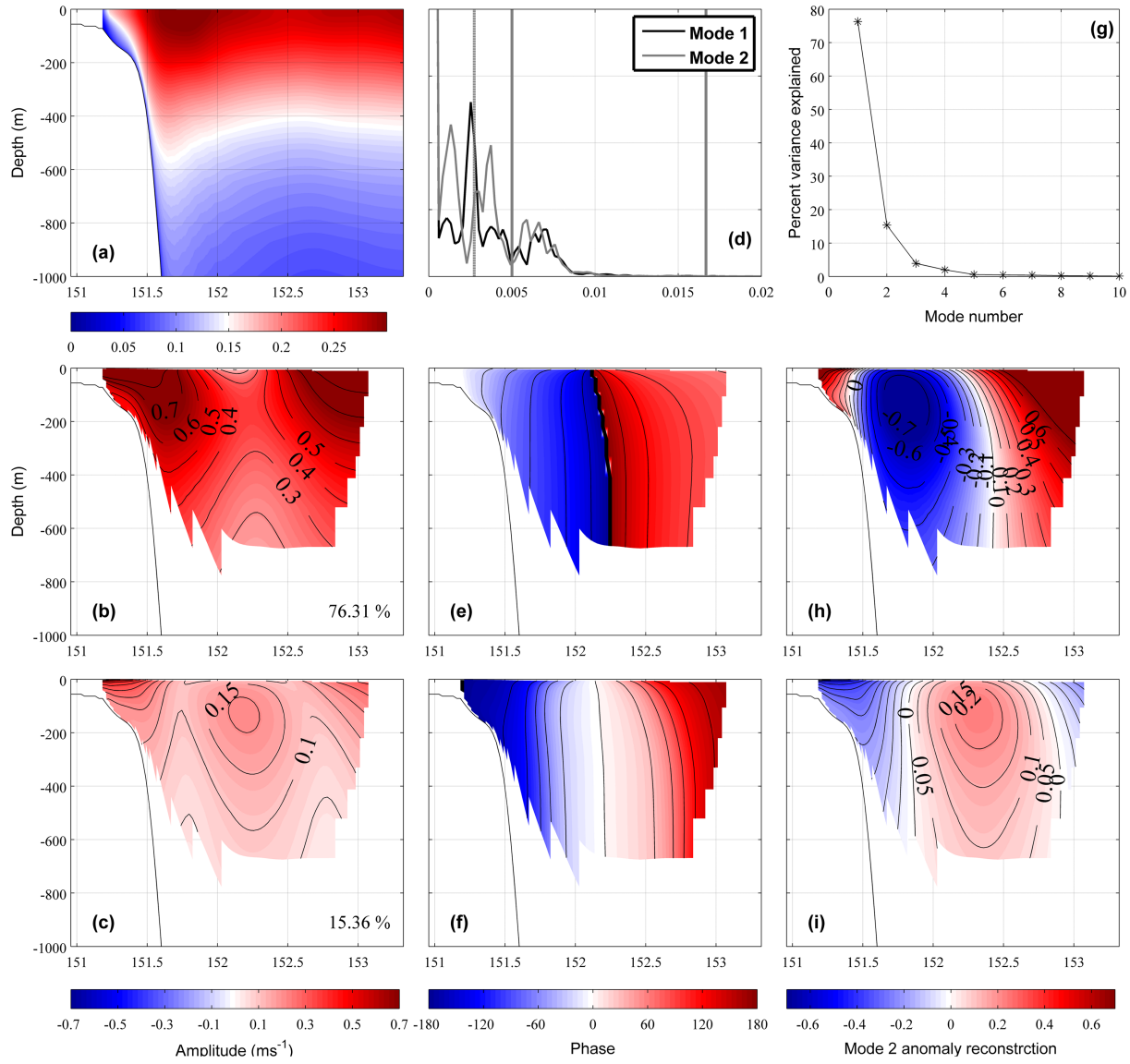

Figure 13. As above for the 33.9° S cross section.

The phase of the seasonal cycle (Figure 9c) changes from 145° at 27° S to 200° at 32° S, corresponding to a lag of about 55 days. The greatest rate of increase occurs from 30° S to 32° S encompassing the latitudinal range over which separation occurs most often. As presented in section 5.1, at 27.5° S the EAC has its strongest poleward transport in mid-December and weakest in mid-June, while at 30.3° S there is a lag of about 2 weeks with the strongest and weakest occurring during late December and late June, respectively. At 32.3° S, the strongest poleward transport occurs in mid-February and the weakest in mid-August. At 34° S, the phase returns to close to that preseparation; the current that continues poleward south of the separation latitude from 34° S to 35° S has an annual cycle that is in phase with the poleward current to the north of the separation latitude. The amplitude of the seasonal cycle decreases between 35° S and 36° S and corresponds to a shift-change in the phasing of the seasonal cycle over this latitudinal range.

7. Complex Empirical Orthogonal Function analysis

7.1. EAC 3-D Velocity Structure

To characterize the subsurface structure of the EAC, we apply time domain complex empirical orthogonal function (CEOF) analysis to alongshore velocity for cross-shore sections through the current core. CEOF analysis is useful for detecting propagating signals. We analyze alongshore velocity for the five cross-sections

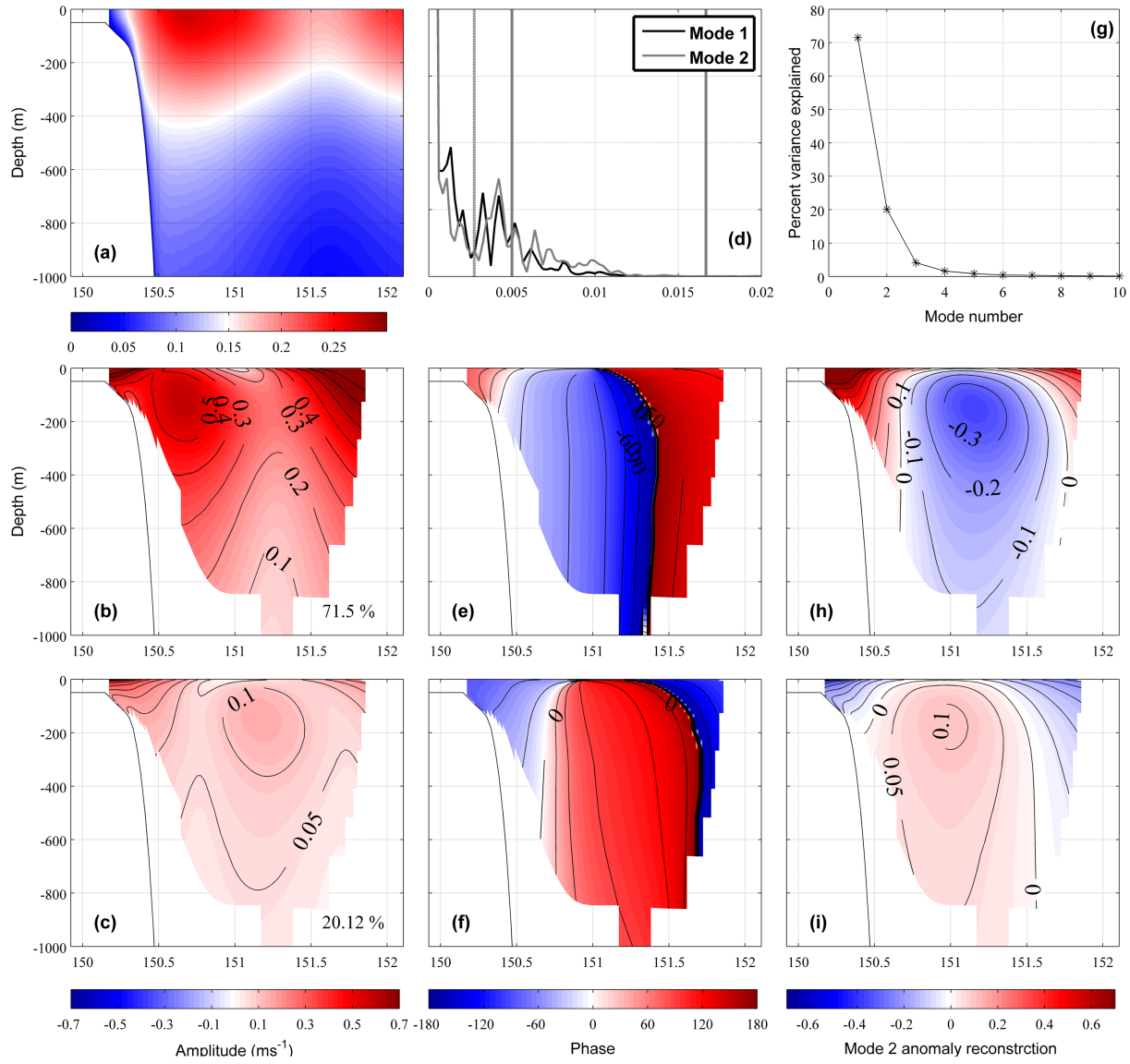

Figure 14. As above for the 36.2° S cross section.

(off Brisbane (27.5° S), Coffs Harbour (30.3° S), Forster (32.3° S), Sydney (33.9° S), and Narooma (36.2° S), shown in Figures 2a and 2b) over the cross-sectional region through which the main EAC jet flows, as defined by the area inside the −0.05 ms^{-1} contour in the alongshore velocity mean. To study variability at intra-annual timescales typically associated with the mesoscale circulation, we band-pass filter the alongshore velocity between 60 and 200 days (consistent with the timescales of mesoscale variability shown in Archer et al., 2017; Bowen et al., 2005; Wilkin & Zhang, 2007) using a fourth-order Butterworth filter. The band-pass filter is applied as CEOF analysis is more accurate for narrow-banded signals, to avoid the representation of unphysical modes (Merrifield & Guza, 1990).

The Hilbert transform is applied to the band-passed alongshore velocity to create complex time series of the data and retain phase information. Empirical orthogonal functions (EOF) are computed from the covariance of the Hilbert transformed time series to generate spatial maps of the amplitude and phase of each EOF mode, and time series of their variation. The analysis is presented in Figures 10–14. For each section, the plots show the standard deviation of alongshore velocity band-pass filtered at 60–200 days, the amplitude, phase, and anomaly reconstruction for Modes 1 and 2 of the CEOF analysis, and the frequency spectra of the amplitude temporal expansion functions of Modes 1 and 2. The anomalies are reconstructed from the spatial maps of amplitude (A) and phase(θ) by $A \times (Sin\theta + Cos\theta)$. Plots of percentage variance explained

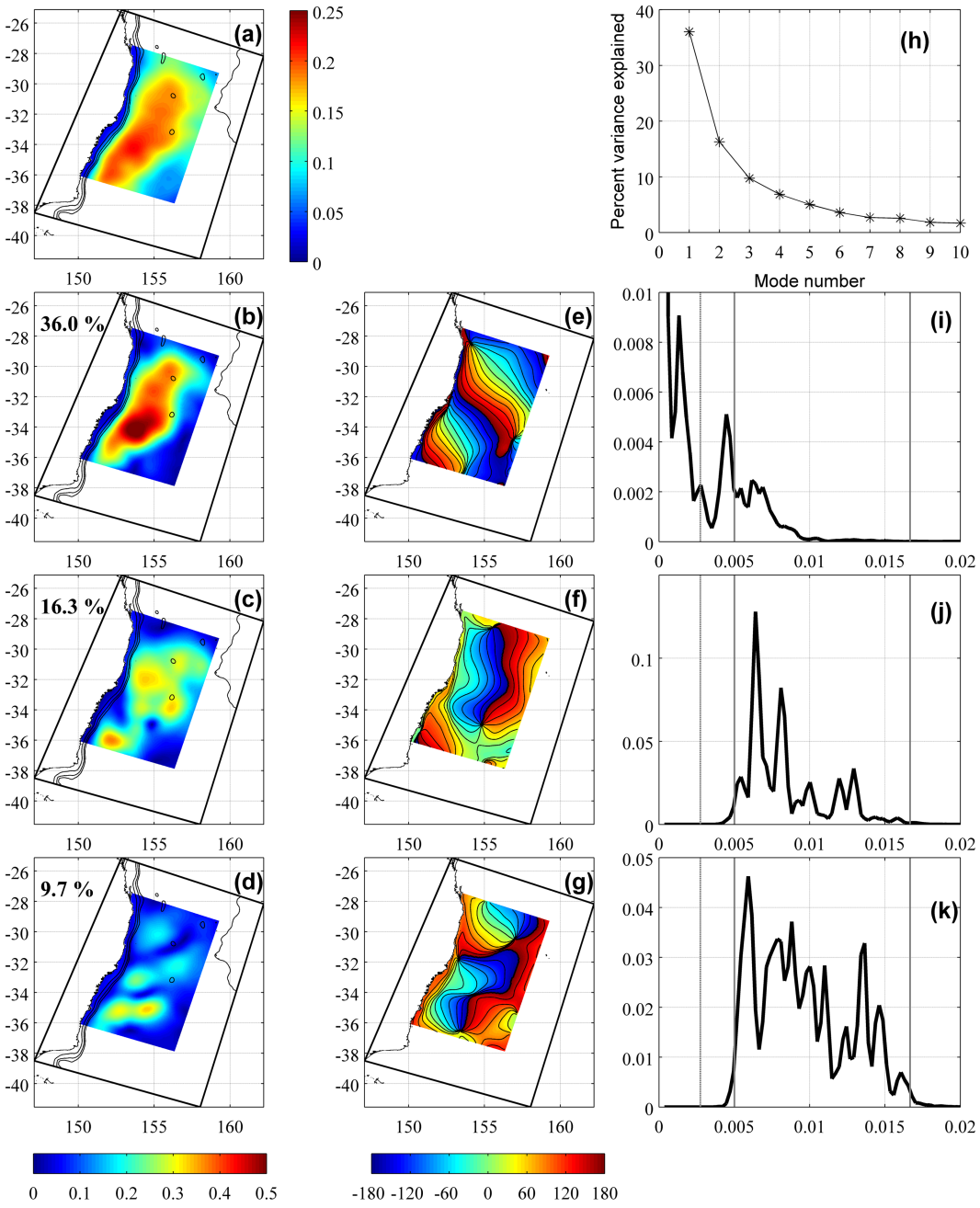

Figure 15. Complex EOF modes for SSH bandpass filtered at 60–200 days. (a) Standard deviations of the filtered SSH. (b–d) Spatial expansion function amplitude of Modes 1–3 and (e–g) phase of Modes 1–3 . The percentage variability explained by each mode is shown on the amplitude plots. A scree plot (h) shows the percent variance explained against mode number. (i–k) Frequency spectra of the temporal expansion functions of Modes 1–3. The vertical gray lines on the spectra show, from left to right, the frequencies corresponding to the annual period, to 200 days, and to 60 days.

against mode number (scree plots Jolliffe, 2002) for each section indicate that the first two modes should be retained (Figures 10–14g).

The sum of the first two modes describe 83.8%, 88.6%, 86.3%, 91.7%, and 91.6% of the variability in alongshore velocity for the Brisbane, Coffs Harbour, Forster, Sydney, and Narooma cross-sections, respectively. Interestingly, the structure of the spatial expansion plots for amplitude and the reconstructed anomalies for the first two modes are similar across all five sections. For all sections, the first CEOF mode for alongshore velocity describes equatorward flow over the continental shelf and shelf break, a poleward flowing EAC over

the continental slope extending offshore and a return flow on its offshore edge. Mode 1 describes 68% of the variability of Brisbane, 77% off Coffs Harbour, 71% off Forster, 76% off Sydney, and 72% off Narooma. Mode 2 describes poleward flow centered over the continental shelf slope, with a flow reversal in the middle of the latitudinal extent of the section, and poleward flow at the offshore extent. The superposition of the leading two propagating modes could describe a meandering jet or eddy shedding events.

The temporal expansion function of the amplitude gives information on how the propagating wave amplitude varies with time, and the frequency spectra (Figures 10–14d) reveal the dominant timescales at which the CEOF amplitudes vary. For the Brisbane section, Mode 1 contains most energy at periods greater than a year. Off Coffs Harbour, Mode 1 and Mode 2 peak at the annual period and at ~ 640 days, with Mode 2 also showing a peak at 220 days. Off Sydney, Mode 1 has a dominant peak at the annual period and Mode 2 peaks at 270 and 750 days with a smaller peak at 365 days. Off Forster and Narooma, most of the energy is at periods greater than 200 days.

7.2. Sea Surface Height

CEOF analysis of the SSH fields, band-pass filtered at 60–200 days, reveals information about the source of mesoscale variability (Figure 15). The band-passed SSH data are Hilbert transformed and EOFs are computed from the covariance of the Hilbert transformed time series to generate spatial maps of the amplitude and phase of each CEOF mode. Spectra of the time series of the CEOF modes' variation are computed to show the dominant timescales of variability. The first three modes explain 62% of the SSH variability in the mesoscale eddy related frequency range, with Mode 1 explaining 36%, Mode 2 16%, and Mode 3 10%. Based on the scree plot (Jolliffe, 2002), we choose to retain the first three modes (Figure 15h).

Mode 1 describes variability propagating along the coast (Figures 15b and 15e), representing mesoscale variability stemming from intrinsic instability in the EAC jet. The frequency spectra of the Mode 1 amplitude temporal expansion function (Figure 15i) has most of its energy at periods greater than 200 days, with peaks at 220 and 750 days and a smaller annual peak. The second mode describes westward propagating anomalies (Figures 15c and 15f), consistent with westward propagating Rossby waves (Chelton & Schlax, 1996). The Mode 2 temporal expansion function frequency spectra (Figure 15j) shows most energy is contained between periods of 100–200 days, with peaks at 123 and 156 days. Mode 3 (Figures 15d and 15g) describes bands of SSH variability at the three most common separation regions (~ 30° S, 33° S, and 36° S; refer to Figure 2). The Mode 3 amplitude temporal expansion function (Figure 15k) contains energy across the mesoscale (60–200 day) frequency range.

8. Discussion

Using a long term (22-year), high-resolution (2.5- to 6-km horizontal resolution) hydrodynamic simulation of the EAC system that realistically represents the mean and variability of the circulation, we present the first holistic view of the EAC system, its variability at annual and intra-annual timescales, and the downstream evolution of the current. Characterizing the flows in the EAC system, we show that our model provides further insight into the EAC system inflows and outflows, their variability and interrelationships, and sheds light on the drivers.

8.1. Characteristics of the Mean Flow

On average over the 22 years, 62% of the poleward flow entering the system from the north exits the region via the EAC eastern extension and 38% continues south. This is consistent with Ridgway and Godfrey (1997) and Ypma et al. (2016), who both estimated that about one third of the current's transport continues southward of the separation zone. Transport in the EAC eastern extension and poleward transport from the north (27.5° S) both show a strong peak at annual periods in their frequency spectra (Figures 6a and 6c), and the transports are positively correlated (Figure 6e). The lagged correlation between poleward transport through the northern section and transport in the EAC eastern extension shows spectral peaks at the annual period and at a period of 120 days (Figure 6i), close to the average eddy shedding period of 100 days, indicating a connection between eddy shedding and current transport from the north. This result is consistent with the finding of Sloyan et al. (2016), who suggested that variability of the EAC in the Tasman Sea may be linked to variability upstream of 27° S. Transport in the EAC eastern extension shows a strong negative correlation with the poleward transport in the EAC southern extension (Figure 6f). The anticorrelation between these two currents was referred to as "gating" by Hill et al. (2011), who showed a decadal cycle in the anticorrelation due to shifting of the subtropical gyre in response to basin-wide wind stress curl changes. We show that this

anticorrelation varies at annual periods and at periods of 240 days, about twice the typical eddy shedding period (Figure 6j).

Before separation, the poleward flowing EAC intensifies and deepens as it flows from 27.5° S (mean poleward transport of 19 Sv, jet depth of 800 m, and width of 160 km) toward the typical separation region (32–33.5° S), reaching its maximum depth at 31.5° S (1,300 m) and its maximum mean poleward transport of 26.8 Sv at 32° S (jet depth of 1,230 m and width of 180 km; Figure 9). This downstream strengthening and deepening has also been observed in the Kuroshio by Andres et al. (2017), who used observations taken at two different latitudes and showed that Kuroshio transport increases downstream from 7.3 Sv at 19° N to 13.7 Sv at 24° N with an associated deepening from 750 to 3,000 m. In the Agulhas Current system, Casal et al. (2009) show that the transport increases downstream consistent with the downstream increase in Sverdrup transport.

Historically, a depth of 2,000 m has been used as "level of no motion" in the EAC (e.g., Bowen et al., 2005, and Ridgway & Dunn, 2003). However, our results show that the EAC jet is shallower than previously thought, and thus, we suggest that a level of no motion closer to 1,200 m be adopted. This depth of 1,200 m is consistent with the observations of Sloyan et al. (2016), who showed the mean depth of the current from 2 years of data at a deep mooring array at 27° S. Rykova and Oke (2015) investigated the full depth structure of eddies in the Tasman Sea using thousands of Argo profiles and showed that anticyclonic eddies extend down to approximately 1,500 m whereas cyclonic eddies could have cold temperature anomalies extending to 2,000 m.

The EAC jet separates from the coast between 31.0° S and 34.0° S 50% of the time and between 32.0° S and 33.5° S 38% of the time (Figure 2e). The mean poleward transport reduces over the separation region as a portion of the current turns offshore, with the weakest mean poleward transport of 13.0 Sv occurring downstream of the separation zone at 34.6° S (Figure 9a). The current core shallows over the separation region, from 1,300 m at 31.5° S to 900 m at 34.5° S, and broadens to a maximum core width of 220 km at 33° S. The current core width returns to close to the preseparation magnitude (160 km) south of 35° S (Figures 9d and 9e). Beal and Elipot (2016) show that increased eddy activity in the Agulhas current since the early 1990s has resulted in a broadening of the current.

The EAC transport standard deviation peaks at 22.0 Sv at 32.8° S, poleward of the peak in the mean flow (Figure 9a). The ratio of transport standard deviation relative to the mean poleward transport is considerably greater poleward of the separation latitude (ranging from 0.6 to 0.8 from 27° S to 32° S and 1.1 to 1.4 from 33.5° S to 37° S) indicative of the more eddy-dominated regime. Mean transport gradually increases from 34.6° S (13.0 Sv) to 36.3° S (17.4 Sv), indicating that eddies migrating southwestwards from the Tasman Sea may feed flow in the EAC southern extension. Indeed anticyclonic eddies, which the EAC is known to shed consistently (Bull et al., 2017; Cetina Heredia et al., 2014), most commonly propagate to the south west (Cetina Heredia et al., 2019).

The flow in the EAC eastern extension, between 157.5° E and 159° E, is manifested in two surface-intensified jets evident in the time mean flow fields at 30.6° S (480 m deep) and at 34.0° S (320 m deep; Figure 5i), while the core of the EAC southern extension is 900 m deep at 34.4° S and deepens poleward to 1,300 m at 37° S (Figure 9e). This is consistent with Ypma et al. (2016), who, using a Lagrangian approach, showed that most particles following the EAC eastern extension originate from the top 460 m depth, while most particles following the EAC southern extension originate from depths between 460 m and 1,000 m.

Equatorward flow occurs offshore of the main poleward EAC jet and is broadest close to the separation region (Figures 5a–5e). This equatorward return flow has been observed by mooring arrays at 30° S (Mata et al., 2000) and 27.5° S (Sloyan et al., 2016), XBT and Argo observations at 27° S (Zilberman et al., (2018), and inferred from climatology at 30° S and 32° S (Ridgway & Dunn, 2003; Zilberman et al., 2014). Return flow at depth is also evident at the base of the continental slope (Figures 5a–5e), consistent with short-term observations at 30° S (Mata et al., 2000) and 27.5° S (Sloyan et al., 2016). This deep counterflow has also been observed in the Kuroshio (Andres et al., 2017) and the Agulhas (Casal et al., 2009) currents. An onshore flow feeds into the poleward flowing EAC at 31.0° S (Figures 5g and 5h) due to recirculation, as was described by Ridgway and Hill (2009), strengthening the mean poleward transport (Figure 9a).

8.2. The Seasonal Cycle in Poleward Transport and Eddy Variability

It is well known that the EAC strengthens in the Austral summer, with an associated southward shift in separation latitude (Cetina Heredia et al., 2014; Ypma et al., 2016) and an increase in EKE in the Tasman Sea

(Qiu & Chen, 2004; Ridgway & Godfrey, 1997). Summer time strengthening also occurs in the Agulhas (Beal et al., 2015), the Kuroshio (Rudnick et al., 2011) and the Gulf Stream (Kang & Curchitser, 2016). Our 22-year model simulation shows the amplitude of the EAC alongshore transport seasonal cycle increases poleward toward the separation latitude, from 3.9 Sv at 27.5° S to a maximum of 6.2 Sv at 31.0° S (Figure 9b). The maximum seasonal cycle amplitude is in good agreement with the estimate of Ridgway and Godfrey (1997), who used steric heights derived from in situ observations to show a seasonal amplitude of the EAC of up to 6 Sv. Poleward of the typical separation region, the circulation becomes more mesoscale eddy dominated and the seasonal cycle amplitude is lower (2.7 Sv at 33.5° S). This is consistent with the results of Schaeffer et al. (2014), who showed a stronger annual signal in along-shelf geostrophic current off Coffs Harbour (30° S) than Sydney (34° S), and of Cetina Heredia et al. (2014), who showed annual variability of the poleward transport between 28° S and 34° S, with lower spectral power at annual periods south of 34° S (their figure 10c).

The phase of the seasonal cycle at 32° S lags the upstream seasonal cycle (at 27–30° S) by about 55 days (Figure 9c) This phase lag occurs gradually from 30° S to 32° S, upstream of the typical separation region, and corresponds to the latitudinal range over which the mean poleward transport increases (Figure 9a). At 27.5° S, the EAC has its strongest poleward transport in mid-December and weakest in mid-June, while at 32.3° S, the strongest poleward transport occurs in mid-February and the weakest in mid-August (Table 1 and Figure 7). The phase lag in the seasonal cycle from 30° S to 32° S is about half of the typical eddy shedding period (of 100 days) and supports the understanding that eddies recirculate water and reinforce the transport across 30–32° S. Indeed the poleward transport around 32° S has high variability (Figure 9a) and varies predominately at mesoscale eddy related timescales (Figure 8c). The EKE seasonal cycle is in phase with the seasonal cycle of poleward transport at 32.3° S.

The latitude at which the EAC separates from the coast for the first time migrates southward by about 1° from 31.7° S in June to 32.7° S in January (in phase with the EAC transport annual cycle equatorward of 30° S), with an associated increase in eddy variability in the Tasman Sea about 60 days later. Monthly means of the spatially averaged EKE over the Tasman Sea in the upper 450 m are a minimum in August and a maximum in February (Figure 7f); the difference between the highest and lowest monthly means is 0.021 $m^2\ s^{-2}$ and the amplitude of the annual cycle harmonic fit to spatially averaged EKE is 0.008 $m^2\ s^{-2}$. Scharffenberg and Stammer (2010) use altimetric sea surface height (SSH) data to estimate the annual cycle in EKE at the surface globally and show amplitudes of the annual signal of the order of 0.01–0.03 $m^2\ s^{-2}$ in the EAC region. The amplitude of the annual cycle in EKE in the EAC is of similar magnitude to its southern hemisphere counterparts, the Brazil and Agulhas currents, and less than the annual cycle of EKE associated with the Kuroshio and the Gulf Stream (refer to figure 19 of Scharffenberg & Stammer, 2010). Spatially averaged EKE over the Tasman Sea from our 22-year simulation shows a strong peak in its power spectra at annual periods with relatively little energy in the intra-annual range (Figure 8f), indicating that the average eddy energy over the Tasman Sea is not strongly influenced by individual eddies.

The current that continues poleward south of the separation latitude from 34° S to 35° S has an annual cycle that is in phase with the poleward transport to the north of the separation latitude. The amplitude of the seasonal cycle decreases between 35° S and 36° S and corresponds to a shift-change in the phasing of the seasonal cycle over this latitudinal range. The phasing of the annual cycle in alongshore transport at 36–37° S may be related to the influence of seasonality in the Leeuwin current, which has been hypothesized to drive seasonality off eastern Australia from the south (Oliver & Holbrook, 2018; Ridgway & Godfrey, 1997). The alongshore EAC transport from 36° S to 37° S is weakest in early April, which corresponds to the autumn peak in Leeuwin Current transport (Ridgway & Godfrey, 2015). These results motivate further study into the influence of the Leeuwin Current at these southern latitudes.

8.3. EAC Meanders and Eddy-driven Transport

The intra-annual variability of EAC alongshore velocity over the EAC region was investigated using complex EOF analysis, which allows the identification of propagating modes of variability. The five cross-shore sections analyzed span from where the EAC flows as a mostly coherent jet adjacent to the coast (Brisbane, 27.5° S, and Coffs Harbour, 30.3° S), to the zone where the EAC most frequently separates and becomes eddy dominated (Forster, 32.3° S, and Sydney, 33.9° S), and the EAC southern extension (Narooma, 36.2° S). Across all sections, the structure of the two leading propagating modes of the alongshore velocity in the EAC core at mesoscale eddy related periods (intra-annual, 60–200 days) is similar despite the changing

circulation regime from a meandering EAC jet to an eddy-dominated regime. The superposition of the two leading modes describes either the meandering EAC jet or eddies moving across the EAC core section (Figures 10–14).

Where the EAC is most coherent (27.5° S), the amplitudes of the temporal expansion functions for both Mode 1 and Mode 2 describe the meandering EAC jet and contain most energy at interannual timescales (Figure 10d). The Coffs Harbour section (30.3° S) corresponds to where recirculating eddies begin to contribute to strengthening of the EAC flow (Figure 9a), and the two leading modes of alongshore velocity variability contain energy at interannual periods (similar to the timescale associated with the 27.5° S section) and at annual periods (Figure 11d). Over the EAC separation region, alongshore velocity variability across the sections that are most influenced by eddies shed by the EAC (32.3° S and 33.9° S) is described by two leading modes that vary predominantly at annual timescales (Figures 12d and 13d). In the EAC southern extension (36.2° S), the leading modes describing eddy-driven transport contain energy at periods greater than 200 days with no distinct peak at the annual period. These results suggest that the meandering of the EAC jet varies predominately at periods greater than one year, while the eddy driven transport over the separation region has a strong annual modulation, related to the annual cycle in EKE. Our model shows no apparent seasonality in eddy shedding rates but an annual cycle in both EKE and the strength of eddy driven transport.

Kuroshio meanders, upstream of the current's separation and the formation of the Kuroshio Extension, show variability at periods of a few years to a decade and their presence is related to the strength of the current transport (Kurogi et al., 2013; White & McCreary, 1976). The Kuroshio Extension shows both path changes on interannual timescales and seasonality in its transport and EKE (Qiu, 2002; Yang & Liang, 2018). Shen et al. (2014) show that the Kuroshio transport anomaly east of Taiwan is dominated by mesoscale eddies, indicating annual modulation of the transport related to the annual cycle in eddy variability.

8.4. Mechanisms for Seasonal Variability

The mechanisms for the seasonal variability of the EAC remain unclear. Seasonality in the Agulhas transport has been linked to large-scale circulation in the tropical region forced directly by the wind (Matano et al., 2002). Various machanisms have been suggested to contribute to the seasonal variability in the Kuroshio including external forcing by the monsoon, changes in the North Equatorial Current, fluctuations in volume transport through the Taiwan Strait, and the annual cycle in mesoscale eddy activity (Rudnick et al., 2011). Yang and Liang (2018) show that both barotropic and baroclinic instabilities and external wind forcing are responsible for the seasonal eddy variability in the Kuroshio Extension. In the Gulf Stream, the current's strength and its associated EKE peak in summer and Kang and Curchitser (2016) show that the seasonal cycle is attributed to seasonal buoyancy forcing impacting the flow baroclinic instability and, to a lesser extent, seasonal variability in the local wind forcing.

For the EAC, while the zonal flows in the Coral Sea (15–25° S) do exhibit a seasonal cycle, if this was driving the seasonal cycle in the EAC, we would expect the EAC to be weakest in summer (Ridgway & Godfrey, 1997). Extension of the Leeuwin Current around Tasmania may weaken the EAC in winter, but this mechanism cannot explain the strength of the seasonal cycle in the EAC and the increased seasonal cycle amplitude toward the north. Mesoscale eddies modulate the EAC separation latitude (Cetina Heredia et al., 2014; Mata et al., 2006), with the detachment of eddies causing an abrupt northward retraction of the latitude where the EAC separates, and the development of eddies resulting in a slow southward progression of the separation latitude. Bull et al. (2017) show that increased wind stress variability on timescales shorter than 56 days leads to a poleward shift in the separation latitude and increases in eddy shedding rates and southward eddy propagation. While our model shows stronger poleward EAC flow, a poleward shift in separation latitude and increased EKE in the Tasman Sea in summer, eddies are shed regularly with no apparent seasonality in eddy shedding rates.

Various studies have investigated the response of WBCs to a changing climate, where both the Hadley cell and the midlatitude westerly winds are projected to shift poleward. Oliver and Holbrook (2014) found that for a future climate scenario, involving an increase in wind stress curl east of New Zealand, the EAC showed negligible change in transport north of the separation point but enhanced eddy activity over the Tasman Sea and in the EAC southern extension and increased poleward transport in the EAC southern extension. These changes were also associated with a southward migration of the mean EAC separation point by 0.8° of latitude. Holbrook et al. (2011) demonstrate that ENSO to decadal variations and the multidecadal trend

in observed sea level off southeastern Australia are strongly connected to modulations in EAC transports (over the eddy-dominated region at 34° S) by incoming westward-propagating regional- and large-scale wind stress forced Rossby waves. Beal and Elipot (2016) show that the Agulhas Current has not intensified since the early 1900s but its associated eddy activity has increased. They suggest that intensifying winds in the subtropical gyres may be increasing the EKE of boundary currents, rather than their mean flow. Changes in wind stress over the North Pacific and consequent spin-up of the Kuroshio recirculation gyre are shown to accelerate the northern part of the Kuroshio and Kuroshio Extension (Sakamoto et al., (2005). Upstream of this from the east of Luzon to the south of Japan, Chen et al. (2019) show that the sea surface warming, not the wind change, is the dominant forcing that causes the upper-layer Kuroshio to intensify in a warming climate. Contrary to other WBCs, the Gulf Stream is weakening under climate change. The wind stress change is not the dominant forcing driving the total change of the Gulf Stream, but rather the weak deceleration of the Gulf Stream is due to changes in the Atlantic meridional overturning circulation in response to surface salinity decrease in the high latitudes (Chen et al., 2019).

The mechanisms for increased eddy variability in the EAC and the southward shift in separation latitude under global warming, due to a poleward shift in the subtropical South Pacific wind system, may be a similar mechanism to that driving the seasonality of the EAC system. The interrelationships between the southward shift in separation latitude, the increase in eddy variability in the Tasman Sea and the stronger EAC transport in summer are yet to be fully understood. Indeed, the increase in EKE and strength of the eddy-driven poleward transport in summer may be the driving mechanism for the seasonal cycle of the EAC poleward transport upstream of the separation region. Future work will use our model to investigate the mechanisms for seasonal variability of the EAC.

8.5. Mechanisms for Mesoscale Variability

A number of studies have investigated the drivers of EAC mesoscale variability, however consensus has not been reached over if the variability is predominantly an intrinsic instability of the current system or due to remote forcing. For example, Bowen et al. (2005) suggest that their analyses of propagation and energy, using satellite observations, are consistent with variability generated in the separation region by the current itself and find no evidence for remote forcing at mesoscale related frequencies. Other studies have associated mesoscale variability in the EAC with the westward propagation of Rossby waves across the Tasman Sea from the northern tip of New Zealand (Godfrey et al., 1980; Marchesiello & Middleton, 2000). This idea is supported by recent work by Bull et al. (2018) who show that bathymetric features around New Zealand play a key role in controlling the EAC separation latitude and the mean location of the EAC eastern extension. Holbrook et al. (2011) show that EAC transport is modulated by incoming westward propagating oceanic Rossby waves generated both in the Tasman Sea and remotely (east of New Zealand), accounting for interannual to decadal time scale variations. In the Kuroshio Current system, Klose et al. (2019) suggest that the Rossby waves can "trigger" the internal instabilities, providing a link between the Rossby wave forced view (Qiu & Chen, 2005, 2010) and the internal variability view (Berloff et al., 2007; Pierini et al., 2009).

From our 22-year simulation we show that 62% of the SSH variability at mesoscale eddy related (intra-annual) frequencies can be described by the first three complex EOF modes. The first mode (accounting for 36% of the variability; Figures 15b and 15e) propagates alongshore and describes SSH variability arising from intrinsic instabilities of the EAC jet. The amplitude temporal expansion function for Mode 1 contains most energy at annual to interannual timescales (Figure 15i). This analysis illustrates annual and interannual modulation of the current and its eddy field and suggests that the annual cycle in eddy variability is directly related to the annual cycle in alongshore velocity. The second mode (accounting for 16% of the variability, Figures 15c and 15f) describes a westward propagating signal characteristic of planetary Rossby waves observed at this latitude (Chelton & Schlax, 1996). This mode could represent eddies propagating westward after being shed by the EAC, or Rossby waves from a more remote source, and varies at periods of 100–200 days (Figure 15j). The third mode (Figures 15d and 15g) has amplitude peaks at the three most common separation regions (30° S, 33° S, and 35.5° S; Figure 2e). This mode does not describe a dynamical mechanism for SSH variability at 60–200 day timescales but rather shows eddy shedding with energy across the 60–200 day periods (Figure 15k).

Wilkin and Zhang (2007) apply frequency domain CEOF analysis to the surface velocity stream function (band-pass filtered at 90–180 day periods) from satellite observations and a hydrodynamic model. The spatial patterns of amplitude and phase propagation for the first two CEOF modes computed from satellite data

(their Figure 9b) match closely to the amplitude and phase from our CEOF analysis of modeled SSH variability (Figures 15b,15e and 15c,15f). The spatial patterns of the modes computed from their model (their figure 9a) do not match the patterns from satellite observations or our model as well, as their model boundaries have no energy in the mesoscale band. Specifically, the onshore propagating signal of Mode 2 is present in the CEOF analysis from our model and their analysis of satellite observations, but mostly absent from the analysis of their model, consistent with the Mode-2 variability having a remote source outside of their model domain (east of 162° E). Our Mode-2 frequency spectra contains peaks at 124 and 156 days, consistent with the observed periodicity in the EAC of 90–180 days and the typical eddy shedding frequency of about 100 days. In summary, our analysis suggests that mesoscale SSH variability in the EAC stems from a combination of intrinsic instabilities of the EAC jet and westward propagating Rossby waves from a remote source.

9. Conclusions

While many studies exist using observations and/or models to characterize the EAC at specific latitudes or to study specific processes of interest, differences in study methodologies, observation locations and types, and objectives prevent a holistic view of the EAC system. As such, an overall understanding of the evolution of the EAC along its latitudinal range has been lacking. In order to address the knowledge gaps that exist relating to the mechanisms that drive EAC variability at seasonal (annual) and mesoscale eddy related (intra-annual) timescales, we must first understand the current's alongshore evolution and its annual and intra-annual variability. Furthermore, a thorough understanding of WBC dynamics is crucial to understand and predict their response to a changing climate.

Using the first long term (22-year), high resolution (2.5-6 km horizontal resolution) hydrodynamic simulation of the EAC system, we present an analysis of the surface and subsurface variability across the system at seasonal and intra-annual timescales. We show that the EAC strengthens and deepens as it approaches the typical separation region, the strengthening likely driven by recirculating eddies, reaching a maximum mean poleward transport of 26.8 Sv at 32° S. Over the separation region, 32-33.5° S, the mean current core broadens and shallows, mean poleward transport reduces, and transport standard deviation peaks at 22.0 Sv. The poleward flowing EAC is stronger in the Austral summer, with an associated southward shift in the separation latitude and a higher EKE in the Tasman Sea. The amplitude of the poleward transport seasonal cycle increases toward the separation latitude, reaching a maximum of 6.2 Sv, with a phase shift of about half the eddy shedding period over the separation region. Equatorward of the separation region, the meandering of the EAC jet varies predominately at periods greater than one year, while over the separation region, eddy driven poleward transport has a strong annual modulation, related to the annual cycle in eddy kinetic energy. Mesoscale SSH variability stems from both intrinsic instabilities of the EAC jet, that vary predominantly at periods greater than 200 days, and westward propagating Rossby waves from a remote source, that vary at periods of 100-200 days. Future work will exploit the model to study the mechanisms for the alongshore evolution of the EAC, that drive EAC separation and eddy generation and that result in the seasonal variability of the EAC.

Acknowledgments
This research and Dr. C. Kerry were partially supported by an Australian Research Council Discovery Project 140102337. This work is a contribution to Australian Research Council Industry Linkage Grants 160100162 and LP170100498. We used CSIRO Australia BRAN3p5 model output for boundary conditions. We acknowledge the use of Argo data, collected and made freely available by the International Argo Program and the national programs that contribute to it. (https://www.argo.ucsd.edu, https://argo.jcommops.org). The Argo Program is part of the Global Ocean Observing System (http://doi.org/10.17882/42182). We acknowledge AVISO for the Delayed-time SLA data. The Ssalto/Duacs altimeter products were produced and distributed by the Copernicus Marine and Environment Monitoring Service (CMEMS) (https://www.marine.copernicus.eu). SST data was sourced from the Integrated Marine Observing System (IMOS)—IMOS is a national collaborative research infrastructure, supported by the Australian Government and sourced from www.imos.org.au. Model output can be made available for research purposes upon request (https://doi.org/10.26190/5e683944e1369).

References

Andres, M., Mensah, V., Jan, S., Chang, M.-H., Yang, Y.-J., Lee, C. M., et al. (2017). Downstream evolution of the Kuroshio's time-varying transport and velocity structure. *Journal of Geophysical Research: Oceans*, *122*, 3519–3542. https://doi.org/10.1002/2016JC012519

Archer, M., Roughan, M., Keating, S., & Schaeffer, A. (2017). On the variability of the East Australian Current: Jet structure, meandering, and influence on shelf circulation. *Journal of Geophysical Research: Oceans*, *122*, 8464–8481. https://doi.org/10.1002/2017JC013097

Beal, L. M., & Elipot, S. (2016). Broadening not strengthening of the Agulhas Current since the early 1990s. *Nature*, *540*, 570–573.

Beal, L. M., Elipot, S., Houk, A., & Leber, G. M. (2015). Capturing the transport variability of a western boundary jet: Results from the Agulhas Current Time-Series Experiment (ACT). *Journal of Physical Oceanography*, *45*(5), 1302–1324.

Berloff, P. S., Hogg, A. M., & Dewar, W. K. (2007). The turbulent oscillator: A mechanism of low-frequency variability of the wind-driven ocean gyres. *Journal of Physical Oceanography*, *37*, 2362–2386.

Bowen, M. M., Wilkin, J. L., & Emery, B. (2005). Variability and forcing of the East Australian Current. *Journal of Geophysical Research*, *110*, C03019. https://doi.org/10.1029/2004JC002533

Bull, C. Y. S., Kiss, A. E., Jourdain, N. C., England, M. H., & Van Sebille, E. (2017). Wind forced variability in eddy formation, eddy shedding, and the separation of the east australian current. *Journal of Geophysical Research: Oceans*, *122*, 9980–9998. https://doi.org/10.1002/2017JC013311

Bull, C. Y. S., Kiss, A. E., Van Sebille, E., Jourdain, N. C., & England, M. H. (2018). The role of the New Zealand Plateau in the Tasman Sea circulation and separation of the East Australian Current. *Journal of Geophysical Research: Oceans*, *123*, 1457–1470. https://doi.org/10.1002/2017JC013412

CNES (2015). SSALTO/DUACS User Handbook: (M)SLA and (M)ADT Near-Real Time and Delayed Time Products. AVISO Sateliitle Altimetry Data.

Casal, T. G. D., Beal, L. M., Lumpkin, R., & Johns, W. E. (2009). Structure and downstream evolution of the Agulhas Current system during a quasi-synoptic survey in February-March 2003. *Journal of Geophysical Research*, *114*, C03001. https://doi.org/10.1029/2008JC004954

Cetina Heredia, P., Roughan, M., Van Sebille, E., & Coleman, M. A. (2014). Long-term trends in the East Australian Current separation latitude and eddy driven transport. *Journal of Geophysical Research: Oceans*, *119*, 4351–4366. https://doi.org/10.1002/2014JC010071

Cetina Heredia, P., Roughan, M., van Sebille, E., Keating, S., & Brassington, G. B. (2019). Retention and leakage of water by mesoscale eddies in the east australian current system. *Journal of Geophysical Research: Oceans*, *124*, 2485–2500. https://doi.org/10.1029/2018JC014482

Chapman, D. C. (1985). Numerical treatment of cross-shelf open boundaries in a barotropic coastal ocean model. *Journal of Physical Oceanography*, *15*, 1060–1075.

Chelton, D. B., & Schlax, M. G. (1996). Global observations of oceanic rossby waves. *Science*, *272*, 234–238.

Chen, C., Wang, G., Xie, S., & Liu, W. (2019). Why does global warming weaken the Gulf Stream but intensify the Kuroshio? *Journal of Climate*, *32*, 7437–7451.

De Souza, J. M. A. C., Powell, B., Castillo-Trujillo, A. C., & Flament, P. (2015). The vorticity balance of the ocean surface in Hawaii from a regional reanalysis. *Journal of Physical Oceanography*, *45*, 424–440.

Fairall, C. W., Bradley, E. F., Rogers, D. P., Edson, J. B., & Young, G. S. (1996). Bulk parameterization of air-sea fluxes for tropical ocean-global atmosphere coupled-ocean atmosphere response experiment. *Journal of Geophysical Research*, *101*, 3747–3764.

Feron, R. C. V. (1995). The Southern Ocean western boundary currents: Comparison of fine resolution Antarctic model results with Geosat altimeter data. *Journal of Geophysical Research*, *100*(C3), 4959–4975.

Flather, R. A. (1976). A tidal model of the northwest European continental shelf. *Mémoires de la Société royale des sciences de Liège*, *6*, 141–164.

Ganachaud, A., Cravatte, S., Melet, A., Schiller, A., Holbrook, N., Sloyan, B., et al. (2014). The Southwest Pacific Ocean circulation and climate experiment (SPICE). *Journal of Geophysical Research: Oceans*, *119*, 7660–7686. https://doi.org/10.1002/2013JC009678

Godfrey, J. S., Cresswell, G. R., Golding, T. J., Pearce, A. F., & Boyd, R. (1980). The separation of the East Australian Current. *Journal of Physical Oceanography*, *10*, 430–440.

Gordon, A. L., Horai, K. I., & Donn, M. (1983). Southern hemisphere western boundary current variability revealed by GEOS 3 altimeter. *Journal of Geophysical Research*, *88*(C1), 755–762.

Haidvogel, D. B., Arango, H. G., Hedstrom, K., Beckmann, A., Malanotte-Rizzoli, P., & Shchepetkin, A. F. (2000). Model evaluation experiments in the North Atlantic Basin: Simulations in nonlinear terrain-following coordinates. *Dynamics of Atmospheres and Oceans*, *32*, 239–281.

Haney, R. L. (1991). On the pressure gradient force over steep topography in sigma coordinate ocean models. *Journal of Physical Oceanography*, *21*, 610–619.

Hill, K. L., Rintoul, S. R., Ridgway, K. R., & Oke, P. R. (2011). Decadal changes in the South Pacific western boundary current system revealed in observations and ocean state estimates. *Journal of Geophysical Research*, *116*, C01009. https://doi.org/10.1029/2009JC005926

Holbrook, N. J., Goodwin, I. D., McGregor, S., Molina, E., & Power, S. B. (2011). ENSO to multi-decadal time scale changes in East Australian Current transports and Fort Denison sea level: Oceanic Rossby waves as the connecting mechanism. *Deep Sea Reserach II*, *58*, 547–558.

Jolliffe, I. (2002). Principal component analysis, *"Choosing a subset of principal components of variables"* (2nd ed.). Springer.

Kang, D., & Curchitser, E. N. (2016). Seasonal variability of the Gulf Stream kinetic energy. *Journal of Physical Oceanography*, *46*, 1189–1207.

Kerry, C. G., Powell, B. S., Roughan, M., & Oke, P. R. (2016). Development and evaluation of a high-resolution reanalysis of the East Australian Current region using the Regional Ocean Modelling System (ROMS 3.4) and Incremental Strong-Constraint 4-Dimensional Variational (IS4D-Var) data assimilation. *Geoscientific Model Development*, *9*, 3779–3801.

Kerry, C. G., Roughan, M., & Powell, B. S. (2018). Observation Impact in a Regional Reanalysis of the East Australian Current System. *Journal of Geophysical Research: Oceans*, *123*, 7511–7528. https://doi.org/10.1029/2017JC013685

Kistler, R., Kalnay, E., Collins, W., Saha, S., White, G., Woolen, J., et al. (2001). The NCEP/NCAR 50-Year Reanalysis. *Bulletin of the American Meteorological Society*, *82*, 247–268.

Klose, A. K., van Westen, R. M., & Dijkstra, H. A. (2019). Phase synchronisation in the Kuroshio Current system. *Ocean Science Discussions*. https://doi.org/10.5194/os-2019-96

Kurogi, M., Hasumi, H., & Tanaka, Y. (2013). Effects of stretching on maintaining the Kuroshio meander. *Journal of Geophysical Research: Oceans*, *118*, 1182–1194. https://doi.org/10.1002/jgrc.20123

Marchesiello, P., & Middleton, J. H. (2000). Modeling the East Australian Current in the western Tasman. *Journal of Physical Oceanography*, *30*, 2956–2971.

Mata, M. M., Tomczak, M., Wijffels, S. E., & Church, J. A. (2000). East Australian Current volume transports at 30^{o}s: Estimates from the World Ocean Circulation Experiment hydrographic sections PR11/P6 and the PCM3 current meter array. *Journal of Geophyscial Research*, *105*(C12), 28,509–28,526.

Mata, M. M., Wijffels, S. E., Church, J. A., & Tomczak, M. (2006). Eddy shedding and energy conversions in the East Australian Current. *Journal of Geophyscial Research*, *111*, C09034. https://doi.org/10.1029/2006JC003592

Matano, R. P., Beier, E. J., Strub, P. T., & Tokmakian, R. (2002). Large-scale forcing of the Agulhas variability: The seasonal cycle. *Journal of Physical Oceanography*, *32*, 1228–1241.

Mellor, G. L., Ezer, T., & Oey, L. Y. (1994). The pressure gradient error conundrum of sigma coordinate ocean models. *Journal of Atmospheric and Oceanic Technology*, *11*, 1126–1134.

Mellor, G. L., & Yamada, T. (1982). Development of a turbulence closure model for geophysical fluid problems. *Reviews of Geophysics and Space Physics*, *20*, 851–875.

Merrifield, M. A., & Guza, R. T. (1990). Detecting propagating signals with complex empirical orthogonal functions: A cautionary note. *Journal of Physical Oceanography*, *20*, 1628–1633.

Oke, P. R., Brassington, G. B., Griffin, D. A., & Schiller, A. (2008). The Bluelink ocean data assimilation system (BODAS). *Ocean Modelling*, *21*, 46–70.

Oke, P. R., & Middleton, J. H. (2000). Topographically induced upwelling off Eastern Australia. *Journal of Physical Oceanography*, *30*, 512–530.

Oke, P. R., Pilo, G. S., Ridgway, K. R., Kiss, A., & Rykova, T. (2019). A search for the Tasman front. *Journal of Marine Systems*, *199*, 103,217.

Oke, P. R., Roughan, M., Cetina-Heredia, P., Pilo, G. S., Ridgway, K. R., Rykova, T., et al. (2019). Revisiting the circulation of the East Australian Current: Its path, separation, and eddy field. *Progress in Oceanography*, *176*, 102,139.

Oke, P. R., Sakov, P., Cahill, M. L., Dunn, J. R., Fiedler, R., Griffin, D. A., et al. (2012). Toward a dynamically balanced eddy-resolving ocean reanalysis: BRAN3. *Ocean Modelling*, *67*, 52–70.

Oliver, E. C. J., & Holbrook, N. J. (2014). Extending our understanding of South Pacific gyre "spin-up": Modeling the East Australian Current in a future climate. *Journal of Geophysical Research: Oceans*, *119*, 2788–2805. https://doi.org/10.1002/2013JC009591

Oliver, E. C. J., & Holbrook, N. J. (2018). Variability and long-term trends in the shelf circulation off Eastern Tasmania. *Journal of Geophysical Research: Oceans*, *123*, 7366–7381. https://doi.org/10.1029/2018JC013994

Pierini, S., Dijkstra, H. A., & Riccio, A. (2009). A nonlinear theory of the Kuroshio extension bimodality. *Journal of Physical Oceanography*, *39*, 2212–2229.

Qiu, B. (2002). The Kuroshio extension system: Its large-scale variability and role in the midlatitude ocean-atmosphere interaction. *Oceanography*, *58*, 57–75.

Qiu, B., & Chen, S. (2004). Seasonal modulations in the eddy field of the South Pacific Ocean. *Journal of Physical Oceanography*, *34*, 1515–1527.

Qiu, B., & Chen, S. (2005). Variability of the Kuroshio extension jet, recirculation gyre, and mesoscale eddies on decadal time scales. *Journal of Physical Oceanography*, *35*, 2090–2103.

Qiu, B., & Chen, S. (2010). Eddy-mean flow interaction in the decadally modulating Kuroshio extension system. *Deep-Sea Research II*, *57*, 1098–1110.

Ridgway, K. R., & Dunn, J. R. (2003). Mesoscale structure of the mean East Australian Current system and its relationship with topography. *Progress in Oceanography*, *56*, 189–222.

Ridgway, K. R., Dunn, J. R., & Wilkin, J. L. (2002). Ocean interpolation by four-dimensional least squares—Application to the waters around Australia. *Journal of Atmospheric and Oceanic Technology*, *19*(9), 1357–1375.

Ridgway, K. R., & Godfrey, J. S. (1997). Seasonal cycle of the East Australian Current. *Journal of Geophysical Research*, *102*(C10), 22,921–22,936.

Ridgway, K. R., & Godfrey, J. S. (2015). The source of the Leeuwin Current seasonality. *Journal of Geophysical Research: Oceans*, *120*, 6843–6864. https://doi.org/10.1002/2015JC011049

Ridgway, K., & Hill, K. (2009). The East Australian Current. A Marine Climate Change Impacts and Adaption Report Card for Australia 2009, NCCARF Publication.

Rudnick, D. L., Jan, S., Centurioni, L., Lee, C. M., Wang, J., Lee, D.-K., et al. (2011). Seasonal and mesoscale variability of the Kuroshio near its origin. *Oceanography*, *24*, 52–63.

Rykova, T., & Oke, P. (2015). Recent freshening of the East Australian Current and its eddies. *Geophysical Research Letters*, *42*, 9369–9378. https://doi.org/10.1002/2015GL066050

Sakamoto, T. T., Hasumi, H., Ishii, M., Emori, S., Suzuki, T., Nishimura, T., & Sumi, A. (2005). Responses of the Kuroshio and the Kuroshio extension to global warming in a high-resolution climate model. *Geophysical Research Letters*, *32*, L14617. https://doi.org/10.1029/2005GL023384

Saunders, P. M., Coward, A. C., & de Cuevas, B. A. (1999). Circulation of the Pacific Ocean seen in a global ocean model: Ocean Circulation and Climate Advanced Modelling project (OCCAM). *Journal of Geophysical Research*, *104*(C8), 18,281–18,299.

Schaeffer, A., Roughan, M., & Wood, J. E. (2014). Observed bottom boundary layer transport and uplift on the continental shelf adjacent to a western boundary current. *Journal of Geophysical Research: Oceans*, *119*, 4922–4939. https://doi.org/10.1002/2013JC009735

Scharffenberg, M. G., & Stammer, D. (2010). Seasonal variations of the large-scale geostrophic flow field and eddy kinetic energy inferred from the TOPEX/Poseidon and Jason-1 tandem mission data. *Journal of Geophysical Research*, *115*, C02008. https://doi.org/10.1029/2008JC005242

Shchepetkin, A. F., & McWilliams, J. C. (1998). Quasi-monotone advection schemes based on explicit locally adaptive dissipation. *Monthly Weather Review*, *126*, 1541–1580.

Shchepetkin, A. F., & McWilliams, J. C. (2003). A method for computing horizontal pressure-gradient force in an oceanic model with a nonaligned vertical coordinate. *Journal of Geophysical Research*, *108*(C3), 3090. https://doi.org/10.1029/2001JC001047

Shchepetkin, A. F., & McWilliams, J. C. (2005). The regional oceanic modeling system (ROMS): A split-explicit, free-surface, topography-following-coordinate oceanic model. *Ocean Modelling*, *9*, 347–404.

Shen, M. L., Tseng, Y. H., Jan, S., Young, C. C., & Chiou, M. D. (2014). Long-term variability of the Kuroshio transport east of Taiwan and the climate it conveys. *Progress in Oceanography*, *121*, 60–73.

Sloyan, B. M., Ridgway, K. R., & Cowley, R. (2016). The East Australian Current and property transport at 27S from 2012-2013. *Journal of Physical Oceanography*, *46*(3), 993–1008.

Tilburg, C. E., Hurlburt, H. E., O'Brien, J. J., & Shriver, J. F. (2001). The dynamics of the East Australian Current system: The Tasman Front, the East Auckland Current, and the East Cape Current. *Journal of Physical Oceanography*, *31*, 2917–2943.

White, W. B., & McCreary, J. P. (1976). On the formation of the Kuroshio meander and its relationship to the large-scale ocean circulation. *Deep Sea Research and Oceanographic Abstracts*, *23*(1), 33–47.

Whiteway, T. (2009). Australian bathymetry and topography grid. Scale 1:5000000. Geoscience Australia, Canberra.

Wilkin, J. L., & Zhang, W. G. (2007). Modes of mesoscale sea surface height and temperature variability in the East Australian Current. *Journal of Geophysical Research*, *112*, C01013. https://doi.org/10.1029/2006JC003590

Yang, Y., & Liang, X. S. (2018). On the seasonal eddy variability in the Kuroshio extension. *Journal of Physical Oceanography*, *48*(8), 1675–1689.

Ypma, S. L., van Sebille, E., Kiss, A. E., & Spence, P. (2016). The separation of the East Australian Current: A Lagrangian approach to potential vorticity and upstream control. *Journal of Geophysical Research: Oceans*, *121*, 758–774. https://doi.org/10.1002/2015JC011133

Zilberman, N. V., Roemmich, D. H., & Gille, S. T. (2014). Meridional volume transport in the South Pacific: Mean and SAM-related variability. *Journal of Geophysical Research: Oceans*, *119*, 2658–2678. https://doi.org/10.1002/2013JC009688

Zilberman, N. V., Roemmich, D. H., Gille, S. T., & Gilson, J. (2018). Estimating the velocity and transport of western boundary current systems: A case study of the East Australian Current near Brisbane. *Journal of Atmospheric and Oceanic Technology*, *35*, 1313–1329.